

AD-A045 535

MARTIN MARIETTA LABS BALTIMORE MD

F/G 20/4

BOUNDARY LAYER OVER SPINNING BLUNT-BODY OF REVOLUTION AT INCIDE--ETC(U)

AUG 77 K C WANG

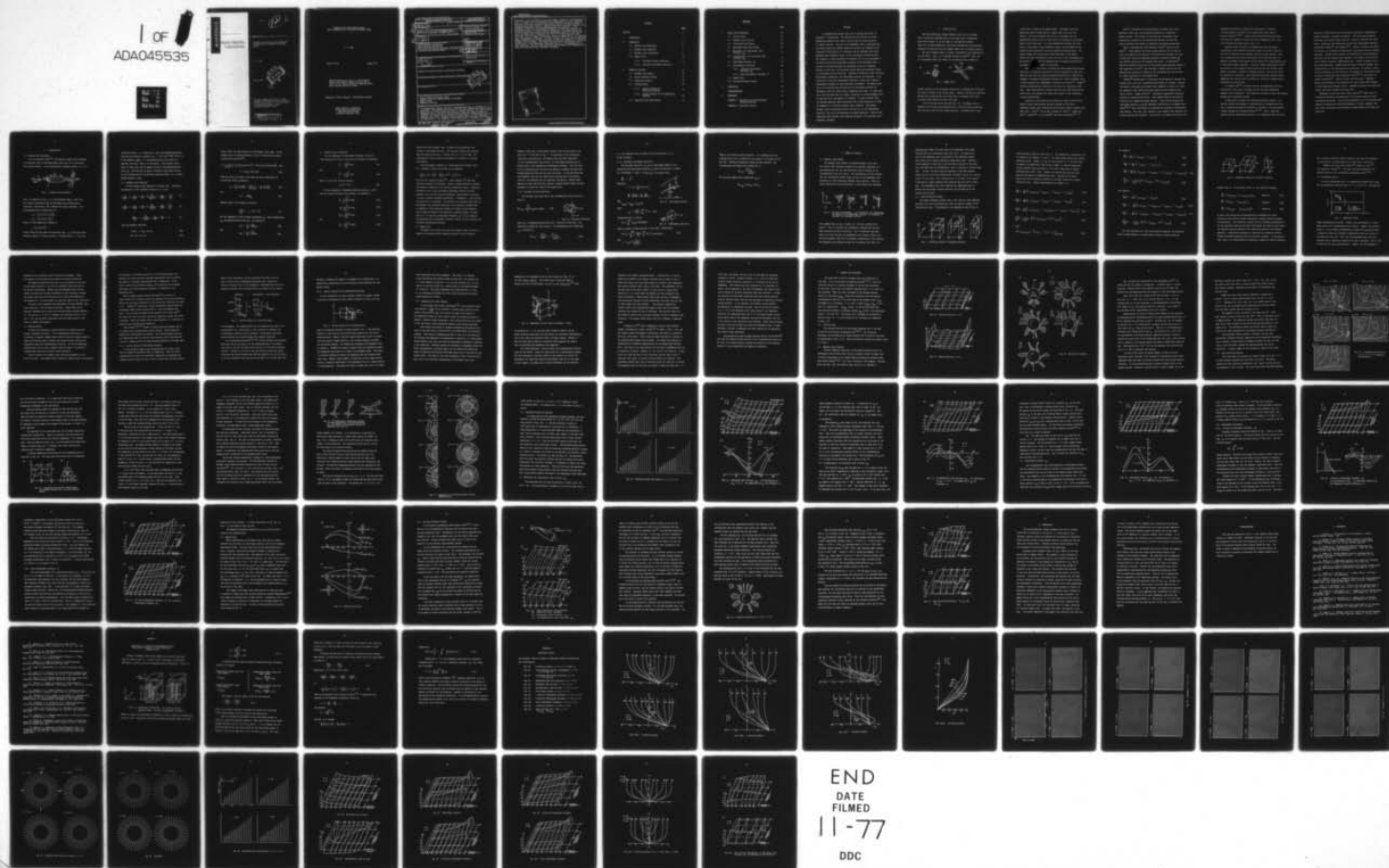
DAHC04-73-C-0011

UNCLASSIFIED

MML-TR-77-50C

NL

1 of  
ADA045535



AD A045535

MARTIN MARIETTA

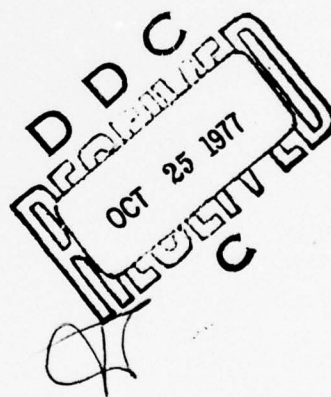
Martin Marietta  
Laboratories

1  
12  
2  
MAIL TR 77-500

BOUNDARY LAYER OVER SPINNING BLUNT-BODY  
OF REVOLUTION AT INCIDENCE AND MAGNUS  
FORCES

K. C. Wang

August 1977



Research sponsored by the U. S. Army  
Research Office under Contract DAE04-73-  
C-0011 and by the U. S. Air Force Office  
of Scientific Research (AFSC),  
Contract F49620-76-C-0004.

**DISTRIBUTION STATEMENT A**

Approved for public release;  
Distribution Unlimited

BOUNDARY LAYER OVER SPINNING BLUNT-  
BODY OF REVOLUTION AT INCIDENCE AND MAGNUS FORCES

K. C. Wang

MML TR 77-50c

August 1977

Research Sponsored by the U. S. Army Research  
Office under Contract DAHC04-73-C-0011 and by  
the U. S. Air Force of Scientific Research (AFSC)  
under Contract F49620-76-C-0004.

Approved for Public Release - Distribution Unlimited

Martin Marietta Corporation  
Martin Marietta Laboratories  
1450 South Rolling Road  
Baltimore, Maryland 21227

REPORT DOCUMENTATION PAGE		READ INSTRUCTIONS BEFORE COMPLETING FORM
1. REPORT NUMBER (14) MML-TR-77-50c	2. GOVT ACCESSION NO.	3. RECIPIENT'S CATALOG NUMBER
4. TITLE (and Subtitle) (6) Boundary Layer Over Spinning Blunt-Body of Revolution at Incidence and Magnus Forces.	5. TYPE OF REPORT & PERIOD COVERED (9) Technical Report	
7. AUTHOR(s) (10) K. C. Wang	6. PERFORMING ORG. REPORT NUMBER MML TR 77-50c	
9. PERFORMING ORGANIZATION NAME AND ADDRESS Martin Marietta Laboratories Martin Marietta Corporation 1450 South Rolling Road, Baltimore, Maryland 21227	8. CONTRACT OR GRANT NUMBER(s)	
11. CONTROLLING OFFICE NAME AND ADDRESS	10. PROGRAM ELEMENT, PROJECT, TASK AREA & WORK UNIT NUMBERS (15) DAHC04-73-C-0011 F49620-76-C-0004	
14. MONITORING AGENCY NAME & ADDRESS (if different from Controlling Office) (12) 90 P.	12. REPORT DATE (11) August 1977	
16. DISTRIBUTION STATEMENT (of this Report)  Approved for public release; distribution unlimited.	13. NUMBER OF PAGES 83	
17. DISTRIBUTION STATEMENT (of the abstract entered in Block 20, if different from Report)	15. SECURITY CLASS. (of this report) Unclassified	
18. SUPPLEMENTARY NOTES	15a. DECLASSIFICATION/DOWNGRADING SCHEDULE	
19. KEY WORDS (Continue on reverse side if necessary and identify by block number) Three-dimensional boundary layer Boundary layer over spinning-body at incidence Magnus forces Numerical solutions		
20. ABSTRACT (Continue on reverse side if necessary and identify by block number) An incompressible laminar flow over a spinning blunt-body at incidence is investigated. The approach follows strictly the three-dimensional boundary layer theory, and the lack of initial profiles is readily resolved. The rule of the dependence zone is satisfied with the Krause scheme and complete numerical solutions are obtained for an ellipsoid of revolution at 6° incidences and two different spin rates. Spinning causes asymmetry which, in turn, introduces the Magnus force. The asymmetry is most pronounced in crossflow, but is also		

407 998



Unclassified

SECURITY CLASSIFICATION OF THIS PAGE(When Data Entered)

noticeable in the skin-friction and displacement thickness of the meridional flow. A variety of crossflow profiles are determined as are the streamline patterns in the cross- and meridional-planes which are especially useful in visualizing the flow structure. Detailed distribution of skin frictions, displacement thicknesses, and centrifugal pressure are presented. A new derivation of the total displacement thickness is given and a negative displacement thickness is found physically meaningful. The Magnus forces due to the crossflow skin friction and the centrifugal pressure are determined; these two forces partly compensate each other. At lower spin rate, the frictional force is larger, resulting in a positive Magnus force. At high spin rate, the opposite is obtained. At high incidence ( $30^\circ$ ), the leeside separated region associated with an open separation is found not amenable to a classical boundary layer treatment. The present boundary layer calculations could be carried out, in the longitudinal direction, only up to the beginning of an open separation. Since an open separation moves forward with increasing incidence, the calculable area, therefore, decreases.

ACCESSION for	
NTIS	W. P. Section <input checked="" type="checkbox"/>
DDC	B. H. Section <input type="checkbox"/>
UNANNOUNCED	
JUSTIFICATION	
BY	DIST. TO: <input type="checkbox"/> COPIES
	CIAL
A	

SECURITY CLASSIFICATION OF THIS PAGE(When Data Entered)

## CONTENTS

	<u>Page</u>
ABSTRACT	i
1. INTRODUCTION	1
2. FORMULATION	6
2.1 Geometry and Coordinates	6
2.2 Boundary Layer Equations	7
2.3 Boundary Layer Thicknesses	9
2.4 Magnus Forces	10
2.4 a. Sectional Friction Side-Force	11
2.4 b. Sectional Centrifugal Side-Force	12
3. METHOD OF SOLUTION	14
3.1 Boundary Layer Method	14
3.2 Finite Difference Schemes	15
3.3 Computation Details	19
3.4 Starting Method	20
3.4 a. Initial Profiles for Meridional Marching	21
3.4 b. Initial Profiles for Circumferential Marching	23
3.5 Comparison With Other Methods	24

## CONTENTS

	<u>Page</u>
4. RESULTS AND DISCUSSIONS	28
4.1 Inviscid Input	28
4.2 Boundary Layer Profiles	28
4.3 Cross-plane Flow Pattern	32
4.4 Meridional-Plane Flow Pattern	39
4.5 Meridional (Or Longitudinal) Skin Friction, $c_{f\mu}$	39
4.6 Circumferential (or Cross-flow) Skin Friction, $c_{f\theta}$	42
4.7 Centrifugal Pressure, $p_{ct}$	44
4.8 Displacement Thicknesses	46
4.8 a. v-Velocity Displacement Thickness, $\Delta_{\theta}^*$	46
4.8 b. Total Displacement Thickness, $\Delta^*$	48
4.9 Magnus Force	50
4.10 The High-Incidence Problem	52
5. CONCLUSIONS	58
ACKNOWLEDGEMENTS	60
6. REFERENCES	61
APPENDIX A - Derivation of the Displacement Thickness Equation	63
APPENDIX B - Additional Figures	67

## ABSTRACT

An incompressible laminar flow over a spinning blunt-body at incidence is investigated. The approach follows strictly the three-dimensional boundary layer theory, and the lack of initial profiles is readily resolved. The rule of the dependence zone is satisfied with the Krause scheme and complete numerical solutions are obtained for an ellipsoid of revolution at  $6^\circ$  incidences and two different spin rates. Spinning causes asymmetry which, in turn, introduces the Magnus force. The asymmetry is most pronounced in crossflow, but is also noticeable in the skin-friction and displacement thickness of the meridional flow. A variety of crossflow profiles are determined as are the streamline patterns in the cross- and meridional-planes which are especially useful in visualizing the flow structure. Detailed distribution of skin frictions, displacement thicknesses, and centrifugal pressure are presented. A new derivation of the total displacement thickness is given and a negative displacement thickness is found physically meaningful. The Magnus forces due to the crossflow skin friction and the centrifugal pressure are determined; these two forces partly compensate each other. At lower spin rate, the frictional force is larger, resulting in a positive Magnus force. At high spin rate, the opposite is obtained. At high incidence ( $30^\circ$ ), the leeside separated region associated with an open separation is found not amenable to a classical boundary layer treatment. The present boundary layer calculations could be carried out, in the longitudinal direction, only up to the beginning of an open separation. Since an open separation moves forward with increasing incidence, the calculable area, therefore, decreases.



## 1. INTRODUCTION

The three-dimensional laminar boundary layer over an inclined body of revolution spinning about its own major axis is considered. Aside from interest in its own right as a moving-wall boundary layer flow in three dimensions, this kind of problem has long attracted attention in connection with the 'Magnus effect' for a flying projectile.

The idea of Magnus effect is usually introduced in the literature as the lift force,  $\rho \Gamma V_\infty$ , on a rotating circular cylinder<sup>(1)</sup> (Fig. 1a). It is presented within the context of a potential flow in terms of a

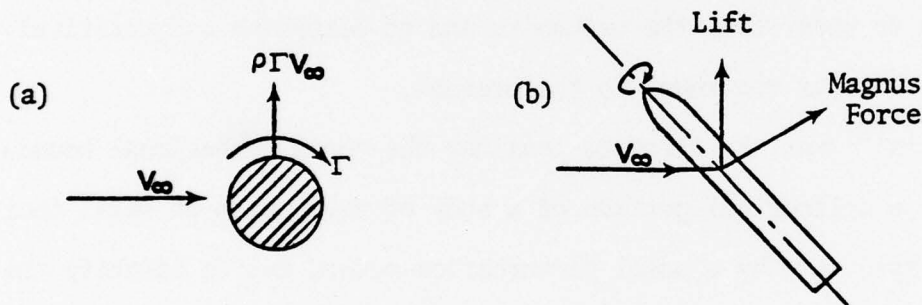


Fig. 1. Magnus Force.

uniform velocity  $V_\infty$  and an assumed circulation  $\Gamma$ , although the circulation was noted to be due to the viscous effect. However, the precise connection between the circulation and the viscous flow (or boundary layer flow) has always been difficult to make very clear.

For an inclined finite long body (Fig. 1b), the Magnus force is defined to be the side-force perpendicular to the lift plane (containing the lift vector and the free stream velocity). The moment due to such

a side-force is known as the Magnus moment. The Magnus force and moment may cause a flying object to depart from its pre-set trajectory. The cross-sectional view of Fig. 1b resembles the two-dimensional picture of Fig. 1a, but this way of looking at the problem doesn't really help much. In a three-dimensional problem, the circulation is not always a very convenient concept, and the Magnus forces could be better analyzed in terms of surface-distributed forces. The question about what surface force would contribute to the Magnus effects and their calculability turns out to be a very challenging one. Our search to understand the mechanism and to determine quantitatively the Magnus effects continues to the present.

Martin<sup>(1)</sup> was the first to consider the three-dimensional boundary layer over a cylindrical portion of a body of revolution at small incidence and spin rate by a small perturbation method and to identify the asymmetry of boundary displacement thickness as a source of Magnus force. A similar approach was independently carried out by Kelley<sup>(3)</sup>. Sedney<sup>(4)</sup> further extended Martin's analysis to the case of a supersonic, sharp cone. These investigations correctly point out the right direction for latter work, even though the results were subject to the limitations of small perturbations.

Interest in this problem has resurfaced in recent years and the method of small perturbations has been replaced by the finite-difference method, thus removing the restrictions of small incidence and small spin. Dwyer<sup>(5)</sup> led the way, followed by Clark<sup>(6)</sup>, Vaughn and Reis<sup>(7)</sup>, Watkins<sup>(8)</sup>, Lin and Rubin<sup>(9)</sup> and Dwyer and Sanders<sup>(10, 11)</sup>.

Dwyer<sup>(5)</sup> calculated the three-dimensional boundary layer over a hypersonic sharp cone, but encountered difficulty in obtaining a unique solution. This led him to conclude that the boundary layer equations are invalid for the spinning-body problem, and that the lateral diffusion term should be retained in the governing equations.

Dwyer's contention was later shared by Clark<sup>(6)</sup> and by Lin and Rubin<sup>(9)</sup>. Clark adopted full Navier-Stokes equations for the case of a spinning sphere and an ellipsoid of revolution at incidence, but lack of sufficient resolution apparently presents a difficult problem and very sketchy results for the ellipsoid were given. Lin and Rubin<sup>(9)</sup> employed a parabolicized version of the Navier-Stokes equations similar to that suggested by Dwyer<sup>(5)</sup>; they obtained a complete solution for the spinning cone problem and singled out the circumferential skin friction as a major contribution to the Magnus force.

Watkins<sup>(8)</sup> disputed Dwyer's conclusions and attempted to calculate the boundary layer flow over a spinning ogive-cylinder at incidence. Watkins' insistence on following the boundary layer approach is correct, but there are apparently other difficulties which make his work incomplete with scanty results. Voughn and Reis<sup>(7)</sup> developed an approximate analytical solution for spinning projectiles. Their method should be particularly attractive for engineering design purposes. These authors included the centrifugal pressure as another important contribution to the Magnus force. Dwyer<sup>(10,11)</sup> later reconsidered the spinning cone problem in collaboration with Sanders. This time, they returned to the boundary layer approach, and unique solutions were obtained. In particular, the Magnus force due to the

asymmetric displacement thickness was calculated by a separate inviscid program in contrast to the slender body theory used by previous authors<sup>(2,4,5,9)</sup>. However their modified difference scheme still does not completely satisfy the rule of dependence zone. This will be further discussed later in Sect. 3.5.

Spinning causes reversal of circumferential flow and whether calculation of such reversed flow would violate the initial-value concept for the boundary layer equations has been an open question. Lack of a strong theoretical basis contributes to the confusion about the adequacy of boundary layer theory and the necessity of using parabolicized or full Navier-Stokes equations. Of course, higher approximation offers, in principle, a more complete flow description than the boundary layer theory can provide. However for specific purposes, this may not always be necessary nor desirable. More elaborate formulation requires longer computing time, and may lead to insufficient resolution, making results unreliable and inconclusive.

In related work<sup>(12)</sup>, a similar reversed circumferential-flow was calculated by this author following strictly the three-dimensional boundary layer formulation. This experience convinces us that the spinning problem can be similarly treated.

In this work, we present our detailed methods and results. The specific problem investigated is concerned with an incompressible flow over a spinning ellipsoid of revolution at incidence. The same problem without spinning was considered earlier<sup>(12-14)</sup>. Such a blunt-body problem provides interesting contrasts to the supersonic sharp cone case



previously studied because of the presence of meridional (longitudinal) pressure gradients, favorable and adverse. Lack of pressure gradients would mean less boundary-layer variation. Section 2 describes the formulation, including a new rederivation of the total displacement thickness considered by Moore<sup>(15)</sup> and Lighthill<sup>(16)</sup>. Section 3 explains the method of solution, the rationale of reversed-flow calculation, and the starting procedure. Lack of initial profiles was considered as an insurmountable difficulty for the boundary layer approach, but actually this question can be readily resolved as demonstrated here. Section 4 presents the results and discussions. Complete distributions of various boundary layer characteristics on the spinning body are presented. In contrast, results of the distribution of skin frictions, for example, for the pointed bodies previously studied are either completely absent<sup>(8,9)</sup> or only given at a single crossplane<sup>(10)</sup>. Section 5 gives the conclusions. Appendix A details the derivation of the equations for total displacement thickness in three-dimensional boundary layers. Appendix B provides more calculated results than those included in the main text.

Highlights of this work were briefly reported<sup>(17)</sup> before with restricted distribution; the preparation of the present report has been interrupted and delayed. This work was presented at the 14th International Congress of Theoretical and Applied Mechanics at Delft, September 1976. More recent calculations have extended the same problem to the high incidence case.

## 2. FORMULATION

### 2.1 Geometry and Coordinates

As in our previous study<sup>(12)</sup>, the specific example of an ellipsoid of revolution (Fig. 2) with minor/major axes ratio of 1/4 was chosen for concrete results. A non-rotating body coordinate system,  $\mu$ ,  $\theta$ ,  $z$  is

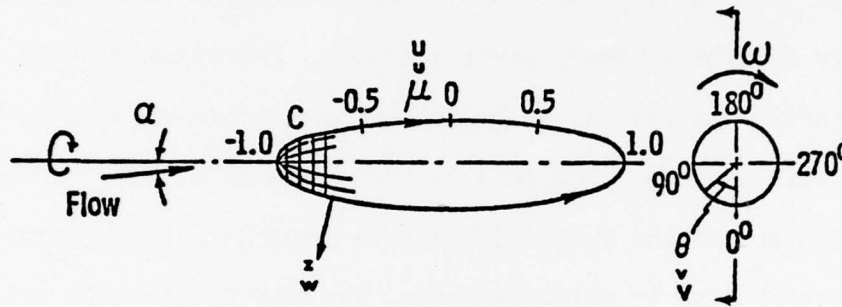


Fig. 2. Geometry and Coordinates.

used. As depicted in Fig. 2,  $\alpha$  is the incidence angle,  $\mu$  and  $\theta$  are two surface coordinates along the meridional and circumferential directions, respectively, and  $z$  denotes the normal coordinate. The corresponding metric coefficients are

$$h_{\mu} = \left[ (1 - e^2 \mu^2) / (1 - \mu^2) \right]^{1/2},$$

$$h_{\theta} = \left[ (1 - e^2) (1 - \mu^2) \right]^{1/2},$$

where  $e$  is the eccentricity defined by

$$e = \left[ 1 - (b/a)^2 \right]^{1/2},$$

$a$  and  $b$  being the semi-major and semi-minor axes.  $h_{\theta}$  is just the cross-sectional radius at a fixed  $\mu$ -station. We shall denote  $u$ ,  $v$ ,  $w$  as the

velocities along  $\mu$ ,  $\theta$ ,  $z$  directions;  $u$  and  $v$  are non-dimensionalized with the flow velocity at infinity  $V_\infty$ ;  $w$  with  $V_\infty/R^{1/2}$  where  $R(=V_\infty a/\nu)$  is the Reynolds number;  $z$  is non-dimensionalized with  $a/R^{1/2}$ ; the pressure, with  $\rho V_\infty^2$ , where  $\rho$  is the density. The ellipsoid spins about its major axis with an angular velocity  $\omega$  non-dimensionalized with  $V_\infty/a$ . The direction of spin is clockwise viewed from the rear. All the variables are in the physical, primitive form; i.e., no transformed variable is used.

## 2.2. Boundary Layer Equations

A strict boundary layer approach is followed here. The governing equations in the coordinate system of  $\mu$ ,  $\theta$ ,  $z$  are

$$u \frac{\partial u}{h_\mu \partial \mu} + v \frac{\partial u}{h_\theta \partial \theta} + w \frac{\partial u}{\partial z} - v^2 \frac{\partial h_\theta}{h_\mu h_\theta \partial \mu} = \frac{-\partial p}{h_\mu \partial \mu} + \frac{\partial^2 u}{\partial z^2}, \quad (1)$$

$$u \frac{\partial v}{h_\mu \partial \mu} + v \frac{\partial v}{h_\theta \partial \theta} + w \frac{\partial v}{\partial z} + uv \frac{\partial h_\theta}{h_\mu h_\theta \partial \mu} = \frac{-\partial p}{h_\theta \partial \theta} + \frac{\partial^2 v}{\partial z^2}, \quad (2)$$

$$\frac{\partial u}{h_\mu \partial \mu} + u \frac{\partial h_\theta}{h_\mu h_\theta \partial \mu} + \frac{\partial v}{h_\theta \partial \theta} + \frac{\partial w}{\partial z} = 0, \quad (3)$$

with the boundary conditions

$$u=w=0, \quad v = \omega h_\theta \quad \text{at } z=0, \quad (4a)$$

$$u=U, \quad v=V \quad \text{at } z \rightarrow \infty, \quad (4b)$$

where  $U$  and  $V$  are the velocities at the boundary layer edge. In the present case of a prolate spheroid,  $U$  and  $V$  are known from an exact inviscid flow solution<sup>(18)</sup>,

$$U = \frac{1}{(1-e^2\mu^2)^{1/2}} \left[ (1+k_a)(\cos\alpha)(1-\mu^2)^{1/2} + (b/a)(1+k_c)(\sin\alpha)\mu\cos\theta \right], \quad (5a)$$

$$V = (1+k_c) \sin\alpha \sin\theta, \quad (5b)$$

where  $k_a$  and  $k_c$  are known as the axial and cross-coefficients of virtual mass and are defined by

$$k_a = \left[ \frac{1}{2e} \log \frac{1+e}{1-e} - 1 \right] / \left[ \frac{1}{1-e^2} - \frac{1}{2e} \log \frac{1+e}{1-e} \right], \quad (6a)$$

and

$$k_c = \frac{1}{1+2k_a}. \quad (6b)$$

Knowing  $U$  and  $V$ , the pressure is given by

$$\frac{p-p_\infty}{\rho V_\infty^2} = 1 - (U^2 + V^2). \quad (7)$$

The two components of skin friction, meridional  $c_{fu}$  and circumferential  $c_{f\theta}$ , non-dimensionalized with  $\rho V_\infty^2$  are defined by

$$c_{fu} = \frac{1}{R^{1/2}} \left( \frac{\partial u}{\partial z} \right)_{z=0}, \quad (8a)$$

and

$$c_{f\theta} = \frac{1}{R^{1/2}} \left( \frac{\partial v}{\partial z} \right)_{z=0}. \quad (8b)$$



### 2.3. Boundary Layer Thicknesses

The two components of displacement thickness,  $\Delta_{\mu}^*$  and  $\Delta_{\theta}^*$ , based respectively on the u- and v-velocity profiles are defined by

$$\Delta_{\mu}^* = \frac{1}{q} \int_0^{\infty} (U-u) dz, \quad (9a)$$

and

$$\Delta_{\theta}^* = \frac{1}{q} \int_0^{\infty} (V-v) dz, \quad (9b)$$

where  $q$  is the total inviscid velocity,

$$q = (U^2 + V^2)^{1/2}. \quad (9c)$$

The four components of momentum thickness, based on u- and v-velocity profiles and their cross products, are defined by

$$\theta_{\mu}^* = \frac{1}{q^2} \int_0^{\infty} (U-u) u dz, \quad (10a)$$

$$\theta_{\theta}^* = \frac{1}{q^2} \int_0^{\infty} (V-v) v dz, \quad (10b)$$

$$\theta_{\mu\theta}^* = \frac{1}{q^2} \int_0^{\infty} (U-u) v dz, \quad (10c)$$

and

$$\theta_{\theta\mu}^* = \frac{1}{q^2} \int_0^{\infty} (V-v) u dz. \quad (10d)$$

Notice that these boundary layer thicknesses are deliberately not written in non-dimensional form. This was done to avoid the situation when the inviscid velocity,  $V$ , becomes zero at  $\theta = 0^\circ$  and  $180^\circ$ . The vanishing of  $V$  does not imply the vanishing of  $v$ -profile in a moving-wall problem.

The displacement thickness of a three-dimensional boundary layer  $\Delta^*$  is defined in terms of  $\Delta_\mu^*$  and  $\Delta_\theta^*$  by the equation:

$$\frac{\partial}{\partial \mu} [h_\theta (U\Delta^* - q\Delta_\mu^*)] + \frac{\partial}{\partial \theta} [h_\mu (V\Delta^* - q\Delta_\theta^*)] = 0. \quad (11)$$

This was first derived by Moore<sup>(15)</sup>. Later Lighthill<sup>(16)</sup> gave four alternative methods of derivation. Moore's original method was included and termed by Lighthill as the "velocity comparison" method. Lighthill's derivation relies on the streamline coordinates formed by the equipotential lines and the inviscid streamlines, whereas Moore's derivation is valid in general orthogonal coordinates. In Appendix A, a new alternative derivation is presented. Our derivation is patterned after that of the ordinary mass continuity equations; the reasoning is somewhat akin to Lighthill's "flow reduction" method, but differs in the formalism. Also it does not depend on the particular coordinate system. We shall refer to  $\Delta^*$  as the total displacement thickness,  $\Delta_\mu^*$  as the  $u$ -velocity (or meridional flow) displacement thickness, and  $\Delta_\theta^*$  as the  $v$ -velocity (or crossflow) displacement thickness.

#### 2.4 Magnus Force

The Magnus force results from the flow asymmetry which, in turn, is caused by the spinning motion through the action of fluid viscosity.

Symmetry refers here to the symmetry plane of the inviscid flow or the plane of  $\theta = 0^\circ$  and  $180^\circ$  of Fig. 2. As mentioned in the Introduction, three major contributions to the Magnus force have been identified: (1) the circumferential skin friction, (2) centrifugal pressure and (3) pressure due to the asymmetrical displacement thickness. Only the first two are determined here; the third one requires a separate inviscid computing program and hence has not been calculated. It has been known that the asymmetric wake vortices shed from an inclined body of revolution even for a non-spinning case also generate side-forces. However determination of these wake vortices requires a complete Navier-Stokes solution and hence is beyond the scope of the present work.

#### 2.4a. Sectional Friction Side-Force

The sectional side-force due to the circumferential skin friction is given by

$$\sqrt{R} F_{sf} = - \int_0^{2\pi} \sqrt{R} c_{f\theta} \cos \theta (h_\theta d\theta), \quad (12a)$$

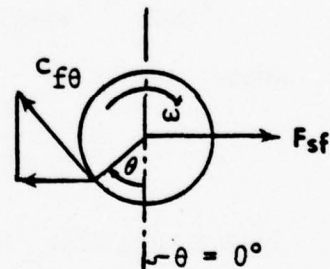


Fig. 3a. Frictional side-force.

where  $F_{sf}$  is nondimensionalized with  $\rho V_\infty^2$ , positive to the right. The subscript *sf* stands for skin friction. A corresponding force coefficient,  $c_{sf}$ , is defined by

$$\sqrt{R} c_{sf} = \frac{\sqrt{R} F_{sf}}{\text{area}} = \frac{\sqrt{R} F_{sf}}{\pi(b/a)^2}, \quad (12b)$$

i.e., the reference area is taken to be the mid-section ( $\mu = 0$ ) of the ellipsoid.

#### 2.4.b. Sectional Centrifugal Side-Force

The sectional side-force  $F_{ct}$  due to centrifugal effects is obtained from the centrifugal pressure  $p_{ct}$  where the subscript ct stands for "centrifugal." After  $v$  is known  $p_{ct}$  is evaluated from,

$$\frac{\partial p}{\partial r} = \frac{v^2}{r}.$$

Replacing

$$r = h_\theta + \frac{z}{\sqrt{R}} \cos \phi \approx h_\theta,$$

$$\frac{\partial p}{\partial r} = \frac{\partial p}{\partial z} \frac{\partial z}{\partial r} = \frac{\partial p}{\partial z} \frac{\sqrt{R}}{\cos \phi},$$

then

$$p_{body} = p_{edge} + p_{ct}/\sqrt{R},$$

where

$$p_{ct} = -\frac{\cos \phi}{h_\theta} \int_0^\infty v^2 dz. \quad (13a)$$

Integrating this, we obtain

$$F_{ct} = -\int_0^{2\pi} p_{body}(\sin \theta) (h_\theta d\theta),$$

where  $F_{ct}$  again is taken positive to the right. Substituting

$$\sqrt{R} F_{ct} = -\int_0^{2\pi} \left[ -\frac{\cos \phi}{h_\theta} \int_0^\infty v^2 dz \right] (\sin \theta) (h_\theta d\theta), \quad (13b)$$

with

$$\phi = \sin^{-1} \left( \frac{\partial h_\theta}{h_\theta \partial \mu} \right).$$

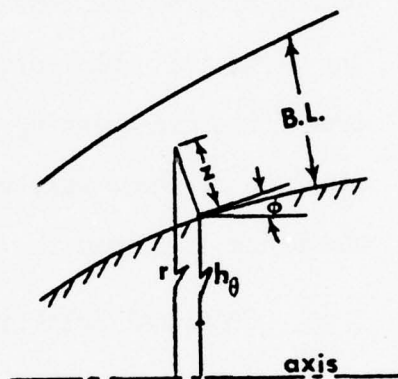


Fig. 3b. Centrifugal pressure.

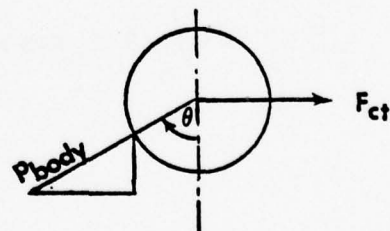


Fig. 3c. Centrifugal side-force.



$p_{\text{edge}}$  is the inviscid surface pressure. It is unaffected by the spinning motion and is symmetrical with respect to the plane of  $\theta=0^\circ$  and  $180^\circ$ . Therefore integration around the body vanishes. The corresponding centrifugal force coefficient is

$$\sqrt{R} c_{ct} = \frac{\sqrt{R} F_{ct}}{\pi(b/a)^2} . \quad (13c)$$

The sectional Magnus-force coefficient  $c_{Mg}$  is

$$\sqrt{R} c_{Mg} = \sqrt{R} c_{sf} + \sqrt{R} c_{ct} . \quad (14) .$$

### 3. METHOD OF SOLUTION

#### 3.1 Boundary Layer Method

The boundary layer method is followed through in this work. This choice comes naturally because of our previous experience in a non-spinning case for the same body where similar reversal of the circumferential flow also occurs. The calculability of such reversed flow was rationalized thereby using the rule of the dependence zone pertaining to three-dimensional boundary layer equations. What are really involved can be seen from Fig. 4, which depicts the dependence

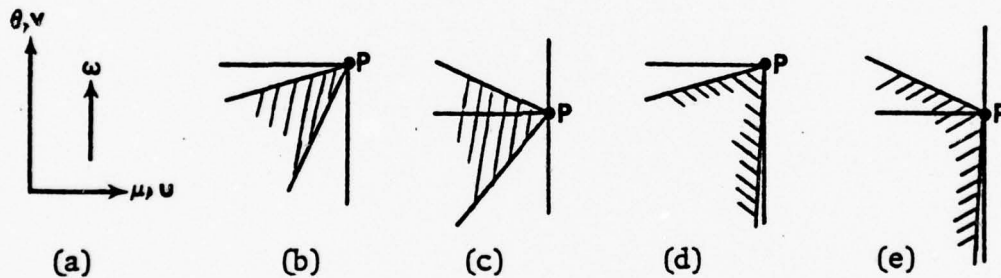


Fig. 4. The zone of dependence. (a) coordinates; (b) nonspinning, no reversal; (c) nonspinning, reversal; (d) spinning, no reversal; (e) spinning, reversal.

zone (shaded area) in the  $\mu$ - $\theta$  plane (i.e. the body surface) for a point P. Fig. 4a indicates the coordinates, assuming that the body spins along the positive  $\theta$ -direction. Fig. 4b indicates that when there is no flow reversal, the dependence zone of point P falls into the third quadrant. When the non-spinning circumferential flow reverses, the dependence zone situates across the  $\mu$ -coordinate line (Fig. 4c).

Spinning merely makes the lower edge of the dependence zone almost coincide with the  $\theta$ -coordinate lines (Fig. 4d,e). As long as the rule of the dependence zone is satisfied by the difference scheme used, there are no logical differences among these cases. Reversal of one component of the flow is not the same as reversal of the total flow, and hence does not automatically lead to violation of initial-value idea. In fact, the flow direction (parallel to the body surface) varies across the three-dimensional boundary layer at a given point on the body, thus sweeping out a certain solid angle. A distinctive, single resultant flow direction does not exist in this case. The dependence rule, which requires the computation mesh to enclose the solid angle, ensures precisely the satisfaction of the initial-value concept.

### 3.2. Finite-Difference Scheme.

The finite difference schemes used in this work are those employed previously for the non-spinning case; they are implicit schemes of the Crank-Nicolson type. Corresponding to the dependence zones of Fig. 4,

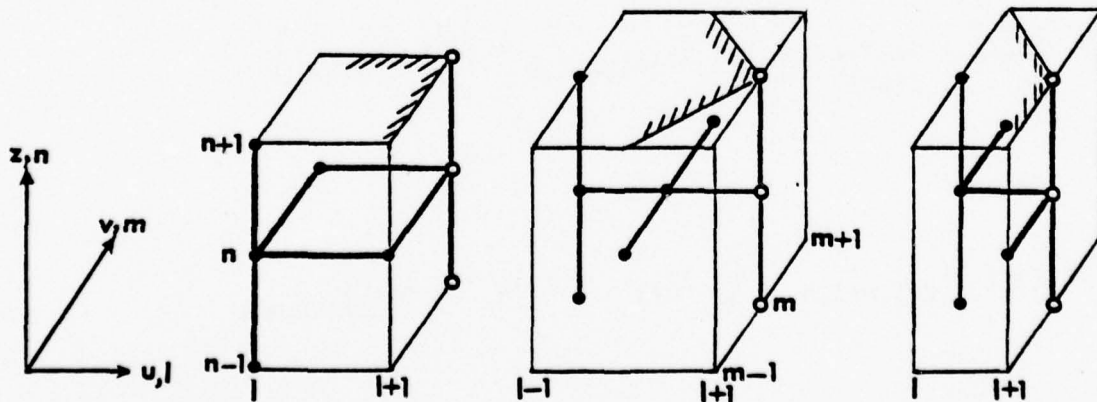


Fig. 5. Difference meshes for momentum equations.

Three different meshes are used (Fig. 5). For convenience, these meshes will be referred to as schemes 1, 2 and 3. The shaded angle denotes each scheme's dependence angle. Scheme 1 is used for area between  $\theta = 0^\circ$  and  $180^\circ$  where no negative circumferential flow occurs; scheme 2 is used for generating initial profiles along the plane  $\theta = 0^\circ$  or  $360^\circ$ , which will be further discussed later (Sect. 3.4b). Scheme 3 is used for the area with both positive and negative circumferential flows. The data at the solid points are used to calculate solutions at the empty circles in a single calculation step. Typical approximations for scheme 1 are

$$\frac{\partial(\quad)}{\partial\mu} = \frac{1}{2\Delta\mu} \left[ (\quad)_{\ell+1,m+1,n} - (\quad)_{\ell,m+1,n} + (\quad)_{\ell+1,m,n} - (\quad)_{\ell,m,n} \right], \quad (15a)$$

$$\frac{\partial(\quad)}{\partial\theta} = \frac{1}{2\Delta\theta} \left[ (\quad)_{\ell+1,m+1,n} - (\quad)_{\ell+1,m,n} + (\quad)_{\ell,m+1,n} - (\quad)_{\ell,m,n} \right], \quad (15b)$$

$$\frac{\partial(\quad)}{\partial z} = \frac{1}{4\Delta z} \left[ (\quad)_{\ell+1,m+1,n+1} - (\quad)_{\ell+1,m+1,n-1} + (\quad)_{\ell,m,n+1} - (\quad)_{\ell,m,n-1} \right], \quad (15c)$$

$$\frac{\partial^2(\quad)}{\partial z^2} = \frac{1}{2(\Delta z)^2} \left[ (\delta^2(\quad))_{\ell+1,m+1,n} + (\delta^2(\quad))_{\ell,m,n} \right], \quad (15d)$$

with

$$(\delta^2(\quad))_{\ell+1,m+1,n} = \left[ (\quad)_{n+1} - 2(\quad)_n + (\quad)_{n-1} \right]_{\ell+1,m+1}. \quad (15e)$$



For scheme 2;

$$\frac{\partial(\quad)}{\partial\mu} = \frac{1}{2\Delta\mu} \left[ (\quad)_{\ell+1,m,n} - (\quad)_{\ell-1,m,n} \right], \quad (16a)$$

$$\frac{\partial(\quad)}{\partial\theta} = \frac{1}{2\Delta\theta} \left[ (\quad)_{\ell,m+1,n} - (\quad)_{\ell,m-1,n} \right], \quad (16b)$$

$$\frac{\partial(\quad)}{\partial z} = \frac{1}{4\Delta z} \left[ (\quad)_{\ell+1,m,n+1} - (\quad)_{\ell+1,m,n-1} + (\quad)_{\ell-1,m,n+1} - (\quad)_{\ell-1,m,n-1} \right], \quad (16c)$$

$$\frac{\partial^2(\quad)}{\partial z^2} = \frac{1}{2(\Delta z)^2} \left[ (\delta^2(\quad))_{\ell+1,m,n} - (\delta^2(\quad))_{\ell-1,m,n} \right]. \quad (16d)$$

For scheme 3;

$$\frac{\partial(\quad)}{\partial\mu} = \frac{1}{\Delta\mu} \left[ (\quad)_{\ell+1,m,n} - (\quad)_{\ell,m,n} \right], \quad (17a)$$

$$\frac{\partial(\quad)}{\partial\theta} = \frac{1}{2\Delta\theta} \left[ (\quad)_{\ell+1,m,n} - (\quad)_{\ell+1,m-1,n} + (\quad)_{\ell,m+1,n} - (\quad)_{\ell,m,n} \right], \quad (17b)$$

$$\frac{\partial(\quad)}{\partial z} = \frac{1}{4\Delta z} \left[ (\quad)_{\ell+1,m,n+1} - (\quad)_{\ell+1,m,n-1} + (\quad)_{\ell,m,n+1} - (\quad)_{\ell,m,n-1} \right], \quad (17c)$$

$$\frac{\partial^2(\quad)}{\partial z^2} = \frac{1}{2(\Delta z)^2} \left[ (\delta^2(\quad))_{\ell+1,m,n} - (\delta^2(\quad))_{\ell,m,n} \right]. \quad (17d)$$

For the calculation of  $w$  from the continuity equation, the derivative  $\partial w / \partial z$  is approximated at a single central station in these respective

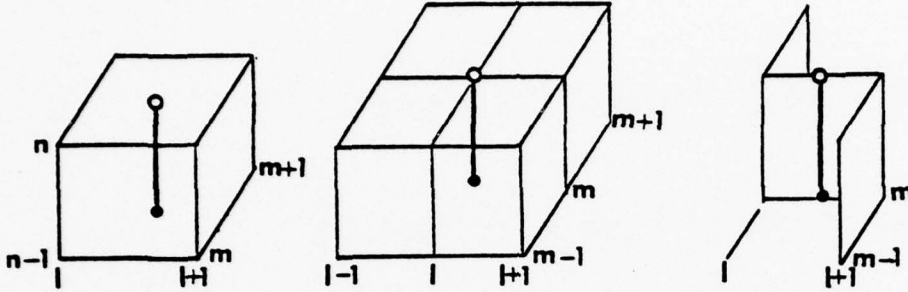


Fig. 6. Difference meshes for continuity equation.

schemes (Fig. 6). As discussed in Ref. 12, this derivative becomes

$$\frac{\partial w}{\partial z} = (w_{l+\frac{1}{2}, m+\frac{1}{2}, n} - w_{l+1, m+\frac{1}{2}, n-1}) / \Delta z, \quad (\text{Scheme 1}) \quad (18a)$$

$$\frac{\partial w}{\partial z} = (w_{l, m, n} - w_{l, m, n-1}) / \Delta z, \quad (\text{Scheme 2}) \quad (18b)$$

$$\frac{\partial w}{\partial z} = (w_{l+\frac{1}{2}, m, n} - w_{l+\frac{1}{2}, m, n-1}) / \Delta z. \quad (\text{Scheme 3}) \quad (18c)$$

At first, this derivative was approximated by averaging over corner stations and was found to exhibit fluctuation, causing eventual breakdown of calculations. Such difficulty results from the difference approximation for the continuity equation and hence falls beyond the scope of usual numerical stability analysis applied to the linearized version of the momentum equations. Linearization decouples or separates the instability problem between the momentum equations and the continuity equation. At the present time, there is no known method for conducting a numerical stability analysis

for a system of nonlinear coupled equations, and hence the difficulty in calculating  $w$  just mentioned has not been clearly understood.

Scheme 1 was first used by Dwyer<sup>(19)</sup>, scheme 2 by Hall<sup>(20)</sup> and scheme 3 by Krause<sup>(21)</sup>. They were previously employed by the present author for the corresponding nonspinning cases<sup>(12,13)</sup>.

### 3.3 Computation Details

As in the nonspinning cases, our computation proceeds first along the circumferential direction from  $\theta = 0$  to  $\pi$  and to  $2\pi$ , and then aft

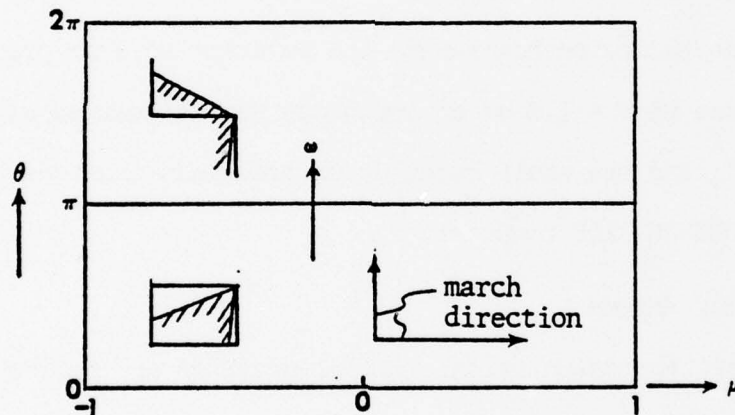


Fig. 7. Computation march.

along the meridional direction. Scheme 1 was used between  $\theta = 0$  and  $\pi$  where there is no circumferential-flow reversal. Scheme 3 was used between  $\theta = \pi$  and  $2\pi$  where circumferential reversed flow always prevails. It should be noted that reversed circumferential-flow also occurs at  $\theta$  less than  $180^\circ$  (say  $120^\circ \sim 180^\circ$ ) for the nonspinning case, but such reversed flow is annulled by opposite flow due to spinning. This is true at least for the case calculated here. Scheme 1 has the advantage of

simplicity and is available from our previous development. Otherwise scheme 3 can alternatively be used for the whole calculation.

The computer program has been built to allow different step-sizes in the normal direction  $z$ , but only two different steps were used in the present calculations. Smaller step was maintained near the body surface to ensure more accurate evaluation of skin frictions, although the results show that skin frictions are not really much affected by the change of  $\Delta z$ . On the average, 50 steps were taken in the  $z$ -direction.

In order to save computing time, experiments of using different step-sizes along the  $\mu$ - and  $\theta$ -direction were made. Larger steps can be employed, depending on how severe the relevant adverse pressure gradient is. The case of  $\omega = 1.0$  at  $6^\circ$  incidence was calculated with  $\Delta\mu = 0.05$  and  $\theta = 10^\circ$ , and the whole calculation took less than one hour of CPU time on a UNIVAC 1108 computer.

### 3.4 Starting Method

To start the calculation, initial profiles are needed along both surface coordinate directions. For a nonspinning inclined body of revolution, a separate boundary-layer solution along the windward symmetry plane has often been used to provide the required initial profiles for computation along the circumferential direction. For the corresponding spinning case, lack of such a symmetry plane and hence its associated boundary-layer solution has caused a major difficulty.

Initial profiles for boundary layer calculation generally do not have to be exact. The boundary-layer problem is a mixed initial- and boundary-



value problem. The boundary-value part of the problem provides some capability for self-correcting reasonably-approximated initial profiles. The adjective "reasonably approximated" must be emphasized. If the initial profiles are arbitrarily picked, the calculation may be doomed, particularly for three-dimensional problems, in comparison to two-dimensional ones.

Lack of symmetry-plane solutions led Dwyer<sup>(5)</sup> to resort to a "guess" method with iteration, which was considered to be semi-satisfactory, except that only some oscillations in the results were found near the plane  $\theta = 0$ . Watkins<sup>(22)</sup> carried out a small perturbation solution about the nonspinning symmetry-plane solution that is valid for moderate spin rates. This was used to develop initial profiles in his later work<sup>(8)</sup>. For large spin rates, the same solution was suggested, coupled with cyclic iterations. Since only sketchy results were presented, it is difficult to judge how this starting method worked out.

Other authors<sup>(9,10,23)</sup> sought to develop difference schemes that do not require such circumferential initial profiles. These alternative methods have objectionable side-effects. The starting methods used here will demonstrate that such initial-value questions can be satisfactorily resolved. Comparisons with the above-mentioned methods will be made later.

#### 3.4.a. Initial Profiles for Meridional Marching

Initial profiles along a fixed crossplane near the vertex of the body are needed for meridional march of computation. Near the vertex, spinning effects have not yet materially changed the corresponding non-spinning profiles except for the v-velocity profile near the body surface.

Based on this observation, initial  $u$ -profiles were taken to be the same as those of the corresponding nonspinning case, whereas the initial  $v$ -profiles (Fig. 8) were obtained by superimposition of the nonspinning  $v$ -profiles with an assumed profile to account for the spinning

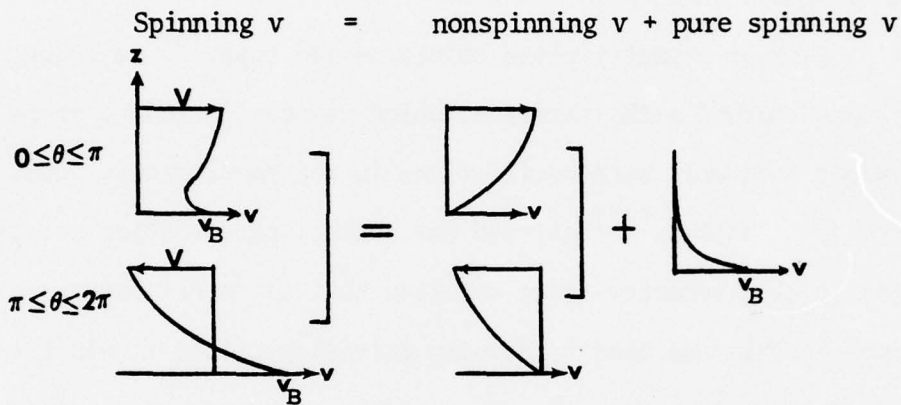


Fig. 8. Initial profile for  $\mu$ -direction march.

of the boundary. The assumed profile in our calculation was taken to be an exponential one. With initial  $u$ - and  $v$ -profiles so obtained, the corresponding  $w$ -profiles can be calculated. Calculations using these initial profiles were started without the slightest difficulty.

In the pointed-body problem<sup>(5,8,9,10)</sup>, initial profiles for meridional march near the tip are taken to be the nonspinning ones on the grounds that since at the tip, the body radius is zero, so is the body's spinning velocity. The fact is, of course, that the initial station must always be located some finite distance away from the geometric tip, and the radius is not only nonzero but also may even be not small as in a blunt body case.

Therefore, although this method is reasonable for a pointed body, our method with a modification for pure spinning is much desirable for more general bodies.

### 3.4.b. Initial Profiles for Circumferential Marching

For the calculation of a new crossplane (fixed in  $\mu$ -plane), scheme 2 was used to determine the first station (station 4 in Fig. 9) at the

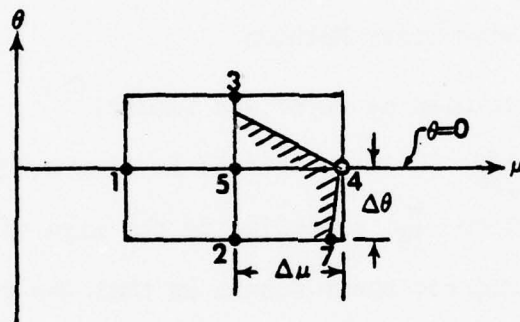


Fig. 9. Initial profile for  $\theta$ -direction march.

plane  $\theta=0$  using the solutions at known stations 1-3, 5. The resulting solution is then used as the required initial profile for the circumferential march. Scheme 2 does not require known data on the  $\mu$ -constant line which passes through station 4, and is hence especially suitable for the present purpose. The shaded area represents the dependence zone of station 4. Evidently the mesh of scheme 2 does not completely enclose the dependence zone unless  $\Delta\mu$  is taken to be extremely small. The latter is certainly impractical because the computing time will become exceedingly long. However, since scheme 2 is used only at this single initial station, incomplete fulfillment of the dependence rule at a single station is inconsequential. Some effort was made to remedy this, but it was found

later unnecessary and hence abandoned. The remedy is as follows:

As the calculation was carried around the body once, the solution for  $\theta = 0$  was compared to that for  $\theta = 2\pi$ , and the solution of  $\theta = 2\pi$  was used as an initial profile for a second round of calculations between  $\theta = 0$  and  $60^\circ$ . Only small differences were found between  $\theta = 0$  and  $\theta = 2\pi$  solutions and between the first round solution and the second round solution for  $0^\circ < \theta \leq 60^\circ$ .

### 3.5. Comparison with Other Methods

In the scheme used by Dwyer and Sanders<sup>(10)</sup>, the crossflow derivative operator ( $v \frac{\partial}{h_\theta \partial \theta}$  in our notation) is always kept positive by evaluating the derivative  $\frac{\partial}{\partial \theta}$  according to the sign of the velocity  $v$ .

One advantage claimed for their scheme is that the convection process is properly modeled; another advantage is that initial-values are not needed in the same fixed- $\mu$  plane passing the unknown station being calculated.

Such change from forward to backward differencing according to the sign of  $v$  has been used in inviscid flow, and indeed models the convection properly. What should be differentiated here is that in an inviscid flow, the influence and dependence are determined by convection; in a three-dimensional boundary layer flow, the same are determined by diffusion in addition to the convection. Diffusion spreads the influence or dependence across the layer instantaneously, and hence smears out the demarcation between the layers of opposing flow-direction from what would occur on the basis of convection alone. The upshot is that this technique is valid in the inviscid case, but is not valid when transplanted to the boundary layer case.



Schematically the dependence zone for the station  $AA_2$  (Fig. 10) is the whole wedge  $AA_2BB_2DD_2$ . The scheme used by Dwyer and Sanders implies that only two sub-wedges,  $AA_1DD_1CC_1$  and  $A_1A_2C_1C_2B_1B_2$ <sup>(23)</sup> need

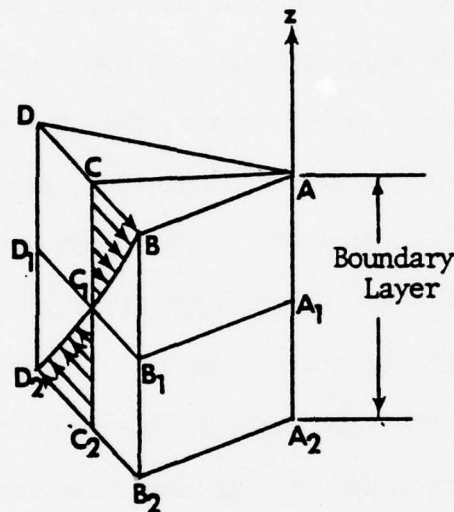


Fig. 10. Dependence zone for Dwyer and Sanders' scheme.

be accounted for. It is true that their scheme is implicit in the normal direction along which all grid points are calculated simultaneously; and in this sense the diffusive nature is loosely modeled. However it does not seem that an implicit calculation would supplant the requirement of satisfying the dependence rule completely.

The second advantage - initial values for circumferential-direction march are not needed - would be a great asset for a spinning-body problem, but such advantage is seriously offset by the inability to satisfy the dependence rule completely unless the meridional step-size is very small. In this respect, the scheme used by Dwyer and Sanders has the identical

problem as our scheme 2 discussed before. In both cases, no initial profiles are needed in the lateral direction and, as shown in Fig. 9, there will always be an area which cannot be covered by the computation mesh unless extremely small steps  $\Delta\mu$  are taken. The difference lies in the fact that in our case, scheme 2 is only used at a single point-station at  $\theta = 0^\circ$ , while Dwyer and Sanders use their scheme for the entire calculation. These authors stated that the rule of dependence zone was grossly violated in their calculation, and their step-size was 10 times larger than that required. They further remarked that "useful results were obtained which agree closely with the converged solutions that obeyed the zone of influence. One possible reason for this behavior could be the very small influence of spin on boundary layer structure." The present author doubts that this statement is generally valid.

Kitchens et al<sup>(23)</sup> made a comparative study of four different schemes, including our earlier version<sup>(13)</sup> of scheme 2 (Sect. 3.4b), and the scheme of Dwyer and Sanders; calculations were made for a parabolic flow over a flat plate. Their study was mainly motivated by interest in the spinning-body boundary layer problem. The scheme they proposed incorporated Lax's difference approximation for one-dimensional unsteady flow. This seems to be a good feature and the rule of dependence zone can be completely satisfied. However, as with Dwyer and Sanders' scheme theirs also uses one-step in the  $\mu$ -direction, and two steps in the  $\theta$ -direction, and, again, no lateral initial-profiles are required. Our preceeding comment about such an advantage versus the inability to satisfy the dependence zone for the Dwyer and Sanders' scheme hold here also. In

both cases, the penalty one has to pay far outweighs the advantage received in return. Secondly Kitchens et al. stress the importance of their scheme being more insensitive to violations of the zone of dependence. They contend that such insensitivity "is important because...strict adherence to the zone of dependence rule could be very costly because of the small downstream step sizes required." Actually the necessity of using small downstream step sizes arises precisely from the adopted scheme, which has the advantage of requiring no lateral initial profiles. In our approach, such lateral initial-profiles are generated, as computation proceeds. Only at the initial station (i.e.  $\theta = 0$ ) is the dependence zone (using scheme 2) not completely covered by the computation mesh; for  $\theta > 0$ , the Krause scheme we used could readily satisfy the dependence zone and the meridional step size is not subject to the restriction just discussed. Rather than stressing how much a particular scheme can violate the dependence zone, it seems preferable, instead, to emphasize how such violation of the dependence rule could be made unnecessary.

The parabolicized Navier-Stokes approach used by Lin and Rubin<sup>(9)</sup> also does not require initial profiles in the circumferential-direction, but this is no bargain because treating the crossflow in an elliptical fashion is a more complicated and expensive alternative.

#### 4. RESULTS AND DISCUSSION

Two cases with  $6^\circ$  and  $30^\circ$  incidence have been calculated in this work. As in our previous non-spinning problem<sup>(12,13)</sup>, these two cases were chosen to illustrate problems at low and high incidences. In each case, results for two different spinning rates ( $\omega = 0.5$  and  $1.0$ ) were obtained. These two rates correspond to the maximum spinning velocity of the body  $(v_B)_{\max}$  being less and greater than the maximum circumferential velocity at the outer edge of the boundary layer,  $V_{\max}$ . For example, at  $6^\circ$  incidence,  $\omega = 0.5$  and  $1.0$  gives  $(v_B)_{\max} / V_{\max} = 0.64$  and  $1.28$ , respectively.  $(v_B)_{\max}$  occurs at the mid-body where the cross-sectional diameter is maximum, whereas  $V_{\max}$  occurs in the meridional planes  $\theta = 90^\circ$  and  $270^\circ$ . The results of  $6^\circ$  incidence are presented in detail in Sect. 4.1 - 4.9; the results of  $30^\circ$  incidence are summarized in Sect. 4.10.

##### 4.1. Inviscid Input

The inviscid solution for the present spinning case is the same as that for the previous nonspinning case<sup>(12,13)</sup>. For convenient reference, the distribution of surface pressure and of inviscid velocities are reproduced in Figs. 11-12. These distributions contain the symmetry plane  $\theta = 0$  and  $\pi$ .

##### 4.2. Boundary Layer Profiles

The most important quantities in the present problem are the circumferential flow profiles which take on a greater variety of shapes than is usually encountered in any single problem including the spinning sharp cone studied before<sup>(9,10)</sup>. Fig. 13a-e illustrate a few examples. Detailed plots for Figs. 13b-e are shown in Figs. B1(a)-(c) of Appendix B.



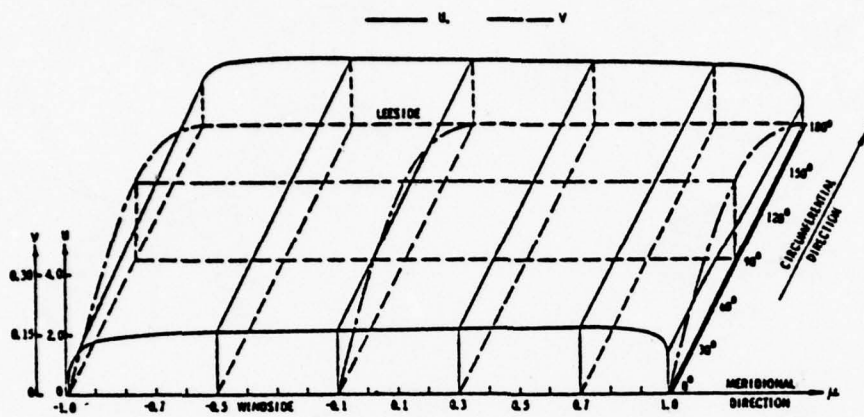


Fig. 11. Inviscid velocity,  $\alpha = 6^\circ$ .

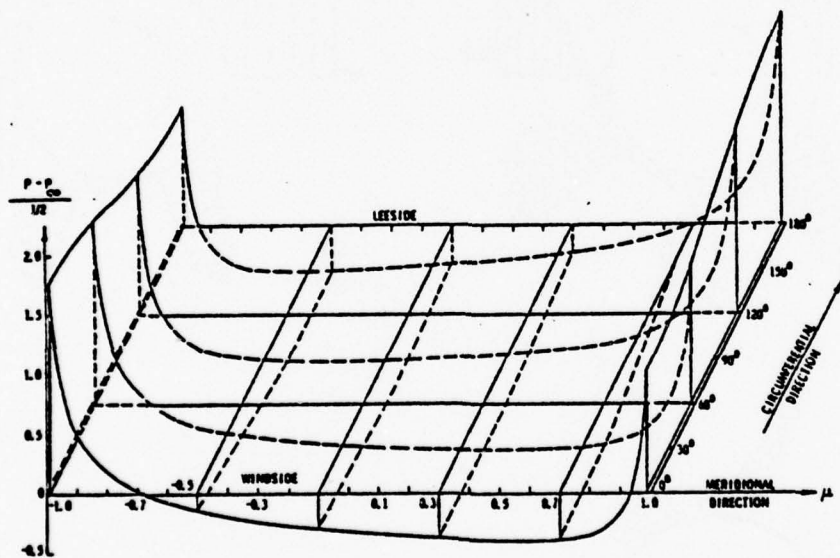


Fig. 12. Surface pressure,  $\alpha = 6^\circ$ .

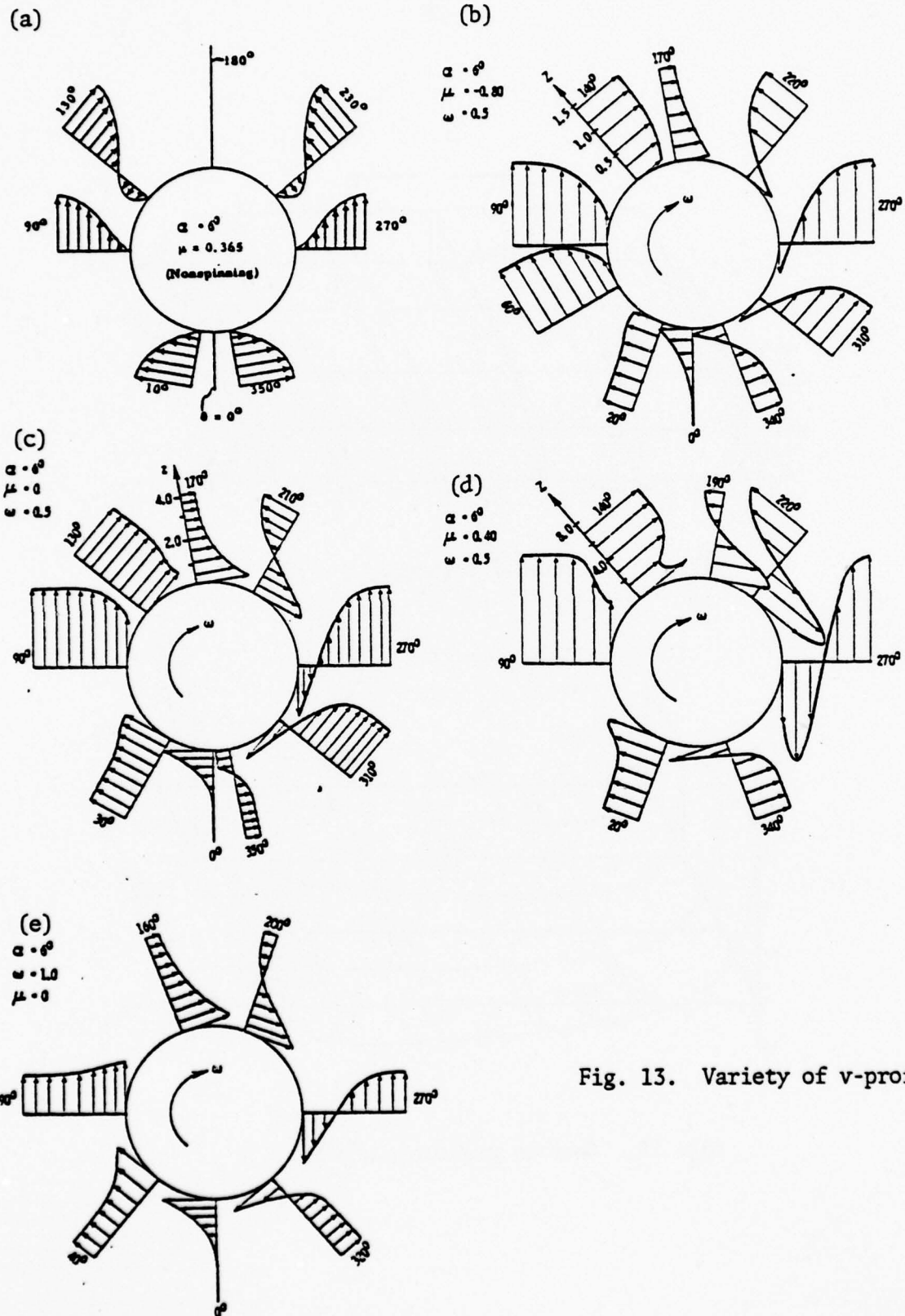


Fig. 13. Variety of v-profile.

Fig. 13a gives the  $v$ -profiles for the nonspinning case<sup>(12)</sup> included here for the purpose of comparison. A symmetry plane is clearly indicated. Reversed flow on the leeside occurs on the aft body. The profiles are non-dimensionalized with respect to local outer-edge velocity.

Figs. 13b-d show the  $v$ -profiles with the spin rate  $\omega = 0.5$  at the fore- ( $\mu = -0.80$ ), mid- ( $\mu = 0$ ) and aft-body ( $\mu = 0.5$ ). For the spinning case, it is more convenient to non-dimensionalize the profiles with respect to  $v_B$ , the spinning velocity of the body.  $v_B$  is equal to  $\omega h_\theta$  and hence varies longitudinally as  $h_\theta$  for a fixed  $\omega$ .

Qualitatively the source of these profile shapes can be visualized by superimposing the nonspinning profile on a pure spinning profile (Fig. 8) and by comparing the velocities  $v_B$  and  $V$ . Consider Fig. 13d, for example, the profile for  $\theta = 20^\circ$  monotonically decrease from the body toward the outer edge with  $v_B$  being greater than  $V$ . That for  $\theta = 90^\circ$  monotonically increases with  $V$  being greater than  $v_B$ . The profiles of  $\theta = 120^\circ, 140^\circ$  are non-monotonic, but always positive, apparently because a strong reversed flow occurs there in the nonspinning case (Fig. 13a). Such reversed flow is opposite to the spinning motion and hence is effectively cancelled out. The profiles for  $\theta = 220^\circ, 270^\circ$  are non-monotonic and reversed while that of  $\theta = 340^\circ$  is monotonic and reversed.

In view of the variety of profile shapes, we have to use the descriptive words "monotonic" and "reversed" to distinguish various cases. "Reversed" means here that the profile contains both positive and negative velocities. In an upstream-moving wall problem including  $\pi \leq \theta \leq 2\pi$  in the present problem, a monotonic reversed profile is fairly common, but a non-

monotonic reversed one (such as that for  $\theta = 220^\circ$ , Fig. 13d) is not; the latter occurs only where a strong reversed flow already exists, even without spinning. Spinning has the effect of reinforcing such reversed flow.

Higher spin rates exert greater influence in shaping the v-profile. This is clearly demonstrated in Fig. 13e for  $\omega = 1.0$  at  $\mu = 0$ . Comparing Fig. 13e to Fig. 13c, it is evident that all profiles in Fig. 13e are monotonically decreasing from the body toward the outer edge, whether they are reversed or not.

The asymmetry of the v-profiles on the right side ( $0^\circ - 180^\circ$ ) with respect to those on the left side ( $180^\circ - 360^\circ$ ) is the major source of Magnus effects. The difference between the profile shape near the body on two sides accounts for the skin frictional contribution to the Magnus force. The difference between the overall shape of those profiles on two sides determines the centrifugal pressure contribution.

The meridional velocity profile, u-profile, does not show particularly different features compared to the corresponding nonspinning ones, although a certain degree of asymmetry between the right and left sides is also noticeable through the coupling between the u- and v-velocities. A typical sample of the u-profiles is shown in Fig. B1(d).

#### 4.3. Cross-Plane Flow Pattern

The cross-plane flow patterns are shown in Figs. 14a-e for  $\omega = 1.0$  at five stations extending from the front to the rear. The arrows indicate the flow direction determined by  $\tan^{-1} (h_0 w/v)$  and the patterns are presented in the  $\theta, z$ -plane. The solid curves drawn therefrom represent



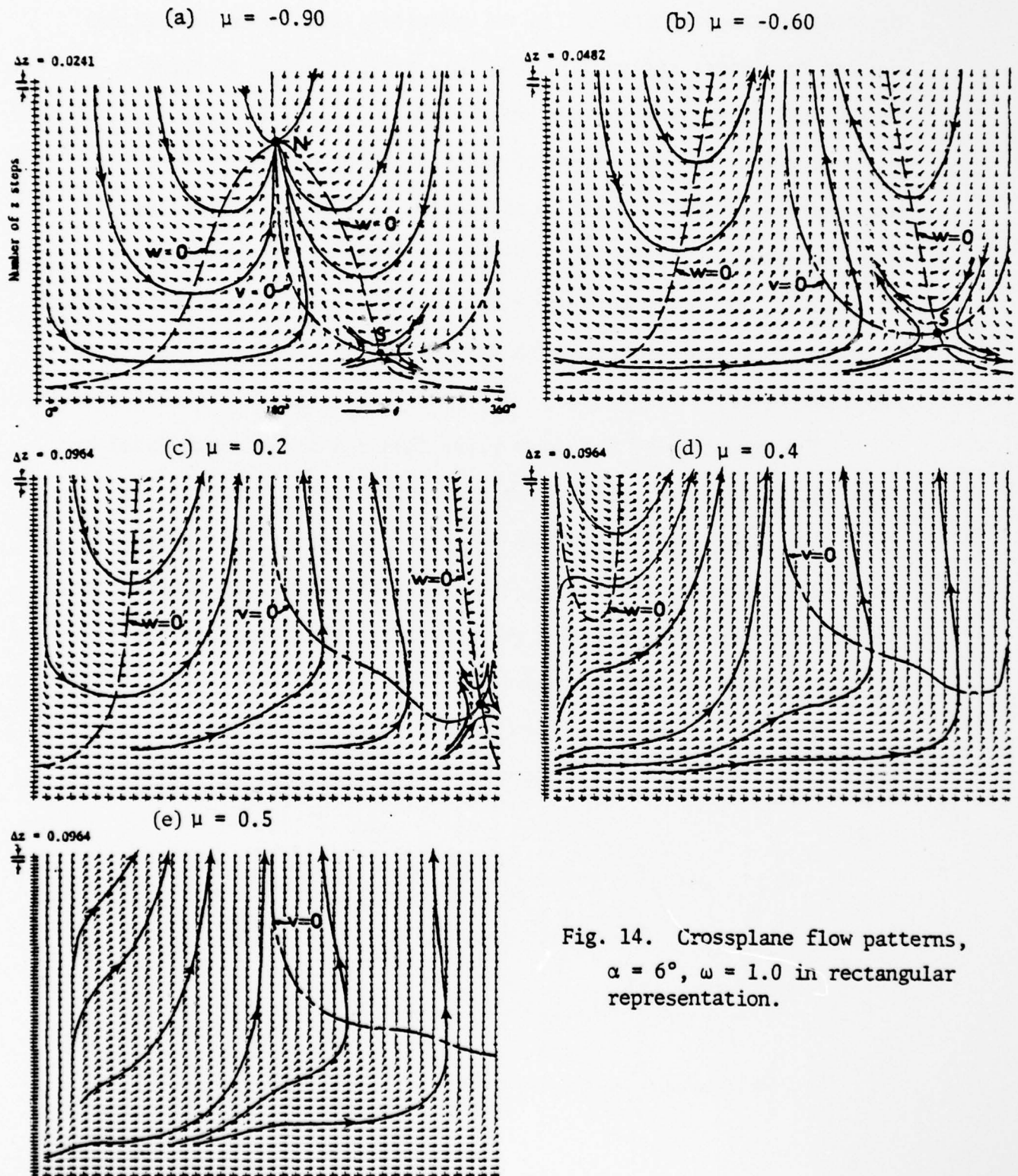


Fig. 14. Crossplane flow patterns,  
 $\alpha = 6^\circ$ ,  $\omega = 1.0$  in rectangular  
 representation.

the cross-plane streamlines. It is understood that these streamlines are not the actual streamlines, but only the projection of three-dimensional streamlines on the cross-plane.

The most obvious effect of spinning is that the flow near the body spins with the body due to viscosity, so that the streamlines (near the body) are parallel or nearly parallel to the body surface. In contrast, the outer portion of the boundary layer is not much affected by spinning so that symmetry with respect to the planes  $\theta = 0$  and  $\pi$  is still preserved.

The structure of the cross-plane flow can be better analyzed by studying the singularities. These are located at the intersection of the curves along which one of the velocity components,  $v$  or  $w$  becomes zero. They are denoted in Figs. 14a - e by the dotted and broken lines. Before we discuss Figs. 14a - e further, let's start with the non-spinning case to provide a comparison.

A typical symmetrical flow pattern for the nonspinning case is depicted in Fig. 15a. The solid lines with arrows are the streamlines

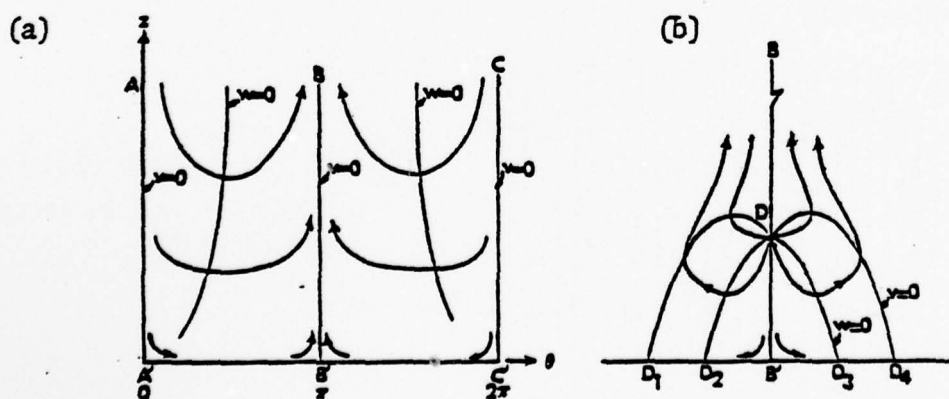


Fig. 15. Crossplane flow pattern (nonspinning);  
(a) without reversed flow, (b) near reversed  
region.

which change from an inflow (toward the body) to an outflow (away from the body) upon crossing the line  $w = 0$ . Along the symmetry-lines  $AA'$ ,  $BB'$ ,  $CC'$ ,  $v$ -velocity vanishes. At the surface  $A'C'$ , both  $v$  and  $w$  vanish. The points  $A'$ ,  $B'$ ,  $C'$  are the saddle points, but  $A'$ ,  $C'$  becomes a nodal point when the cross-plane flow becomes overwhelmingly an outflow in the aft-body. Also, when the circumferential flow reverses on the leeside, a nodal flow pattern develops above the point  $B'$  (Fig. 15b).

Now we return to the spinning case. In Fig. 14a for  $\mu = -0.90$  at the fore-body, the intersection of the curves,  $v = 0$  and  $w = 0$ , determines a nodal point  $N$  and a saddle point  $S$ . The nodal pattern near  $N$  is in the outer portion of the boundary layer and is only slightly affected by spinning so that  $N$  is not located exactly on the plane  $\theta = \pi$  as in the nonspinning case. The saddle pattern around  $S$  is located in the middle of the fluid flow and represents a unique feature of the effect of spin. For comparison, one may think of the curve  $v = 0$  in Fig. 14a corresponding to the line  $BB'C'C$  of Fig. 15a and point  $S$  of Fig. 14a corresponding to point  $B'$  of Fig. 15a. In other words, spinning motion makes the flow asymmetric, shifts the curve  $v = 0$  up, and moves the singularity  $S$  away from the body surface into the fluid.

At  $\mu = -0.60$  (Fig. 14b), the nodal point  $N$  disappears and the curve  $w = 0$  splits into two branches. On the other hand, the curve  $v = 0$  and the saddle point  $S$  are displaced upward and also to the right. Such trends continue up to  $\mu = 0.2$  (Fig. 14c). Here the two branches of the curve  $w = 0$  are further separated, whereas the curve  $v = 0$  and the point  $S$  shift farther upward to the right.

At  $\mu = 0.4$  in the aft-body (Fig. 14d), the two branches of the curve  $w = 0$  join together at the left upper corner. The saddle point disappears altogether and the flow becomes completely outward ( $w > 0$ ) except at the left upper corner. Fig. 14e further indicates that the curve  $w = 0$  completely disappears at  $\mu = 0.50$  so that an outflow prevails over the entire cross-plane. Such pure outflow would have been impossible in a two-dimensional cylinder flow from the viewpoint of mass continuity. It could occur here because of the accompanying meridional (or longitudinal) flow, a three-dimensional effect.

At downstream aft-body stations, the effect of spinning becomes more and more pronounced. Among other factors, this is exhibited by the fact that the layer which spins with the body becomes thicker and thicker (Figs. 14d, e). The layer of such parallel (or nearly parallel) flow increases especially rapidly between  $\theta = 180^\circ$  and  $\theta = 270^\circ$ . This is because the flows from opposite directions collide in that angular region. In particular, the reversed flow which occurs even in the non-spinning case is reinforced by the spinning motion there.

The present problem constitutes an example of a three-dimensional moving-wall boundary layer problem. The two-dimensional moving wall boundary layer problem has been discussed for years by Sears and his associates<sup>(25)</sup> who classify it into downstream-moving (Fig. 16a) and upstream-moving (Fig. 16b) cases. They indicate that the profile and the streamline pattern at separation for the upstream-moving case might appear as depicted in Figs. 16c, d. In our present problem, the crossplane flow involves both a downstream-moving ( $0 \leq \theta \leq \pi$ ) and an upstream-



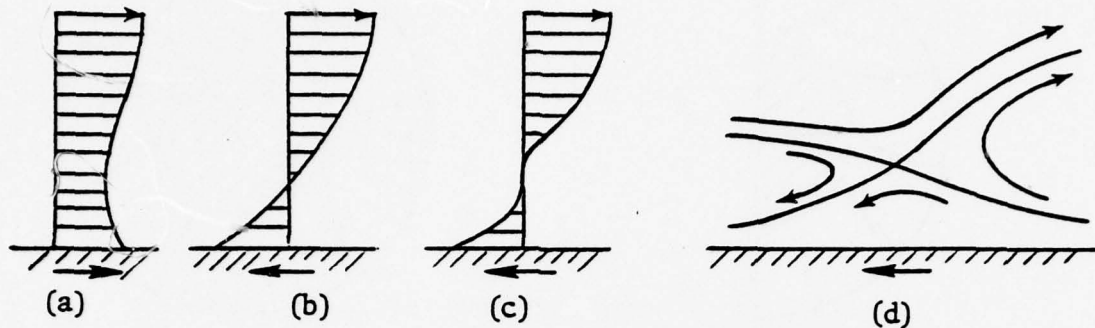


Fig. 16. Two-dimensional moving-wall problem;  
 (a) downstream-moving, (b) upstream-moving,  
 (c), (d) profile and streamline pattern at  
 separation for case (b).

moving ( $\pi \leq \theta \leq 2\pi$ ) wall problem. It is interesting to note that our calculation indeed determines a saddle-point pattern for  $\pi \leq \theta \leq 2\pi$  in Figs. 14a-c, although not much can be said about the connection with respect to flow separation. The separation profile of Fig. 16c has not been found in our crossflow results.

The above crossplane flow patterns may be redrawn around the body's cross sections to give a more physical picture (Fig. 17). Since only a limited number of arrows can be put into such a presentation, the streamline patterns drawn therefrom are necessarily less accurate. The previous nonspinning patterns are also included for comparison. Since the latter is symmetrical, only half of the cross section is shown.

The results presented thus far are for  $\omega = 1.0$ . For the lower spin rate ( $\omega = 0.5$ ), the general trends are similar and the layer which spins with the body is less noticeable. The pattern for  $\omega = 1.0$  at  $\mu = 0.2$

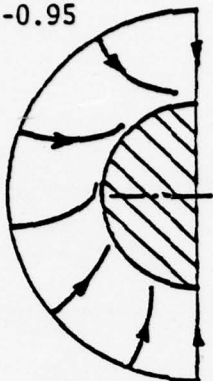
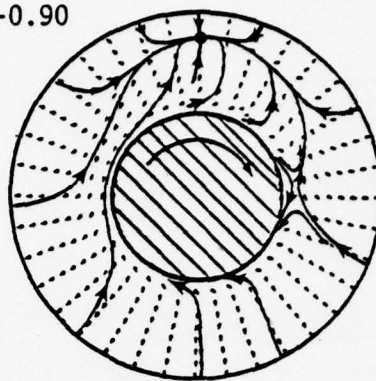
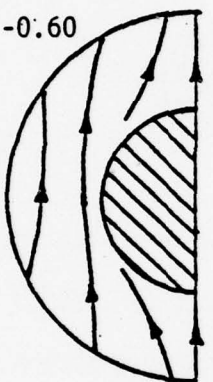
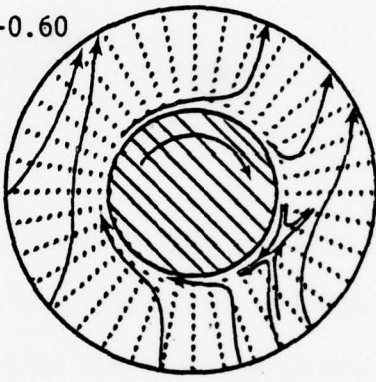
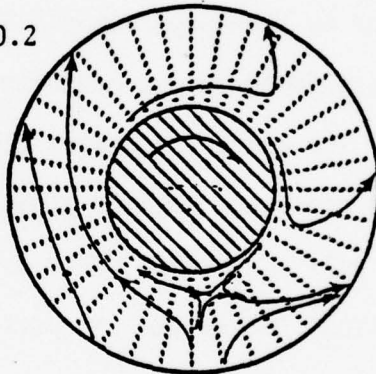
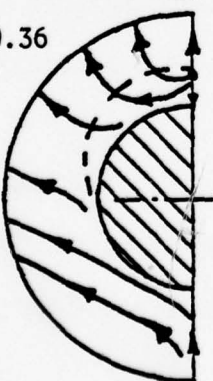
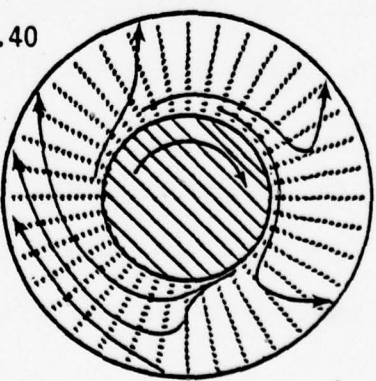
$\omega = 0.5$  $\omega = 1.0$ (a)  $\mu = -0.95$ (a)  $\mu = -0.90$ (b)  $\mu = -0.60$ (b)  $\mu = -0.60$ (c)  $\mu = 0.11$ (c)  $\mu = 0.2$ (d)  $\mu = 0.36$ (d)  $\mu = 0.40$ 

Fig. 17. Comparison of crossflow patterns in polar representation.

looks similar to that for  $\omega = 0.5$  at  $\mu = 0.4$ , implying a lag of the spinning effect. The patterns for  $\omega = 0.5$  are shown in Figs. B2 and B3.

#### 4.4. Meridional-plane Flow Pattern

In conjunction with the preceding crossplane patterns, the flow patterns in fixed meridional planes ( $\theta = 0^\circ, 90^\circ, 180^\circ$ , and  $270^\circ$ ) are also plotted in Figs. 18a - d. The flow direction is given by  $\tan^{-1}(h_\mu w/u)$  and is represented by the arrows in  $\mu$ - $z$  coordinates. A curve along which  $w = 0$  could have been added (but not done here) in Figs. 18a-d to separate area of inflow (with respect to the body) from that of outflow. The calculated longitudinal flow is always pointed downstream (i.e.  $u > 0$ ). From the fore-body toward the aft-body, the flow generally turns increasingly outward. The meridional-plane patterns shown are less complicated than the preceding crossplane patterns. Decrease of  $\omega$  tends to alleviate the outflow in the aft-body, but otherwise similar patterns prevail. The details are shown in Figs. B4. The meridional- and cross-plane flow patterns together help one to visualize the three-dimensional flow structure, although it is difficult to depict the streamline patterns in three-dimensions. When both the cross- and meridional-plane flows become strong outflows, then the resultant flow also must be a strong outflow leading inevitably to the beginning of flow separation.

#### 4.5 Meridional (Or Longitudinal) Skin Friction, $c_{f\mu}$

The meridional skin friction distribution is shown in Fig. 19a for  $\omega = 0.5$ . This distribution is symmetric over the fore body, but be-

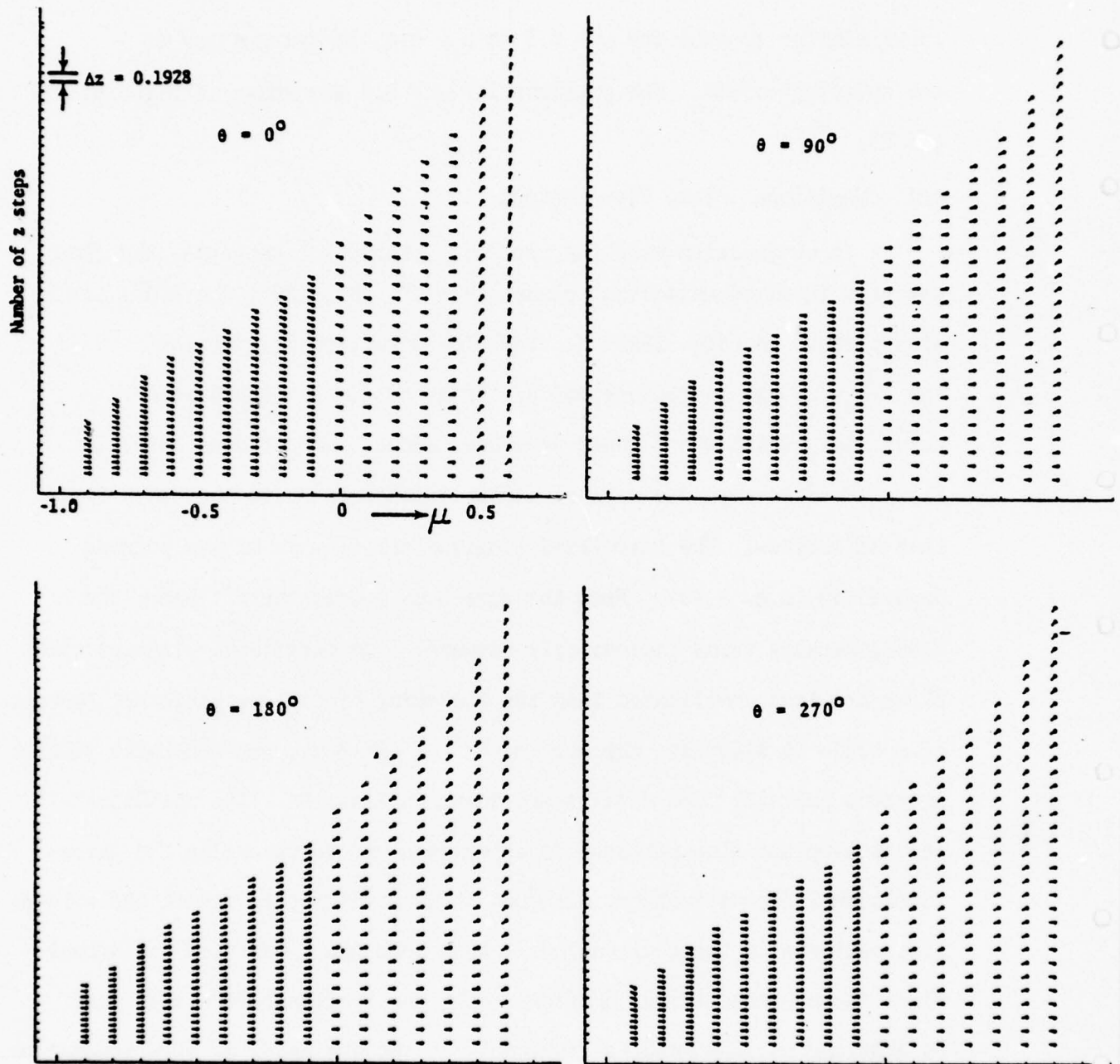


Fig. 18. Meridional-plane flow patterns,  $\alpha = 6^\circ$ ,  $\omega = 1.0$ .



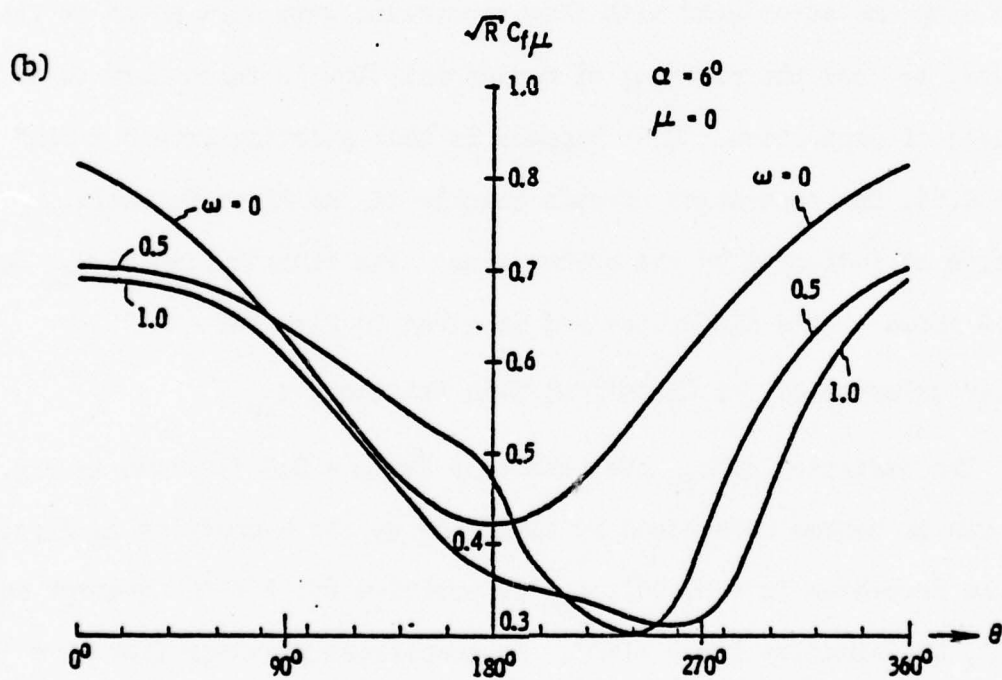
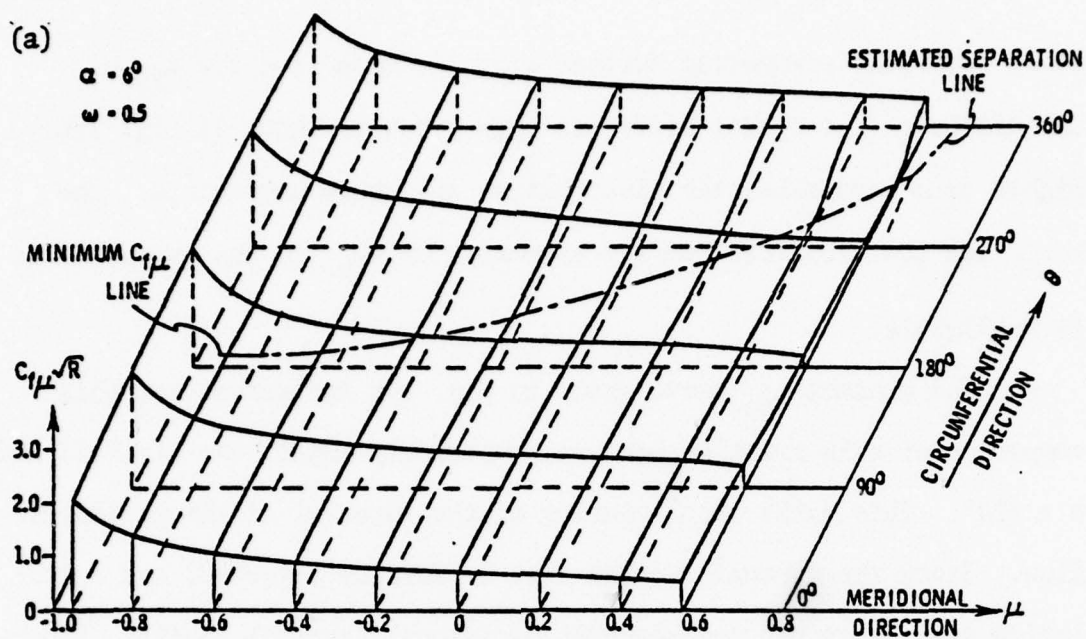


Fig. 19. Meridional skin friction,  $c_{f\mu}$ . (a) Distribution of  $c_{f\mu}$ ,  $\omega = 0.5$ . (b) Comparison of  $c_{f\mu}$  for different  $\omega$ 's.

comes gradually asymmetric further aft. A comparison for  $c_{f\mu}$  at the mid-body ( $\mu = 0$ ) for different spin rates is shown in Fig. 19b. Higher spin rate makes the distribution even more asymmetric. However, the contribution from the asymmetry of  $c_{f\mu}$  to the Magnus force is negligible.

The minimum- $c_{f\mu}$  curve shown in Fig. 19a indicates that this component of skin friction becomes vanishingly small near  $\mu = 0.55$  and  $\theta = 310^\circ$ . This marks the beginning of the reversal of the meridional flow. Since the circumferential flow is already reversed, our calculation must be terminated whenever meridional reversal starts. Other common symptoms associated with flow separation were also noted at the juncture, so that the reversal of meridional flow is taken here to be the onset of separation. What happens is that starting from  $\theta = 310^\circ$  at  $\mu = 0.55$ , the separation spreads quickly in the circumferential direction as indicated by the broken line. The distribution of  $c_{f\mu}$  for  $\omega = 1.0$  shows little difference and is given in Fig. B5.

#### 4.6 Circumferential (or Crossflow) Skin Friction, $c_{f\theta}$

The variation of  $c_{f\theta}$  over the body for  $\omega = 0.5$  is shown in Fig. 20a which can be better understood by referring to the  $v$ -profiles in Figs. 13b-d. Over the fore-body ( $\mu = -0.90$ ),  $c_{f\theta}$  is positive for  $\theta < 180^\circ$  (except near  $\theta = 0^\circ$ ), but negative for  $\theta > 180^\circ$ . At downstream stations (say  $\mu = -0.60$ ),  $c_{f\theta}$  begins to be negative for  $\theta < 180^\circ$ . Farther downstream ( $\mu > 0$ ),  $c_{f\theta}$  becomes positive for  $180^\circ < \theta < 360^\circ$ . This change of sign can be explained by comparing the profiles for  $\theta = 210^\circ$  in Figs. 13c,d. In one case (Fig. 13c),

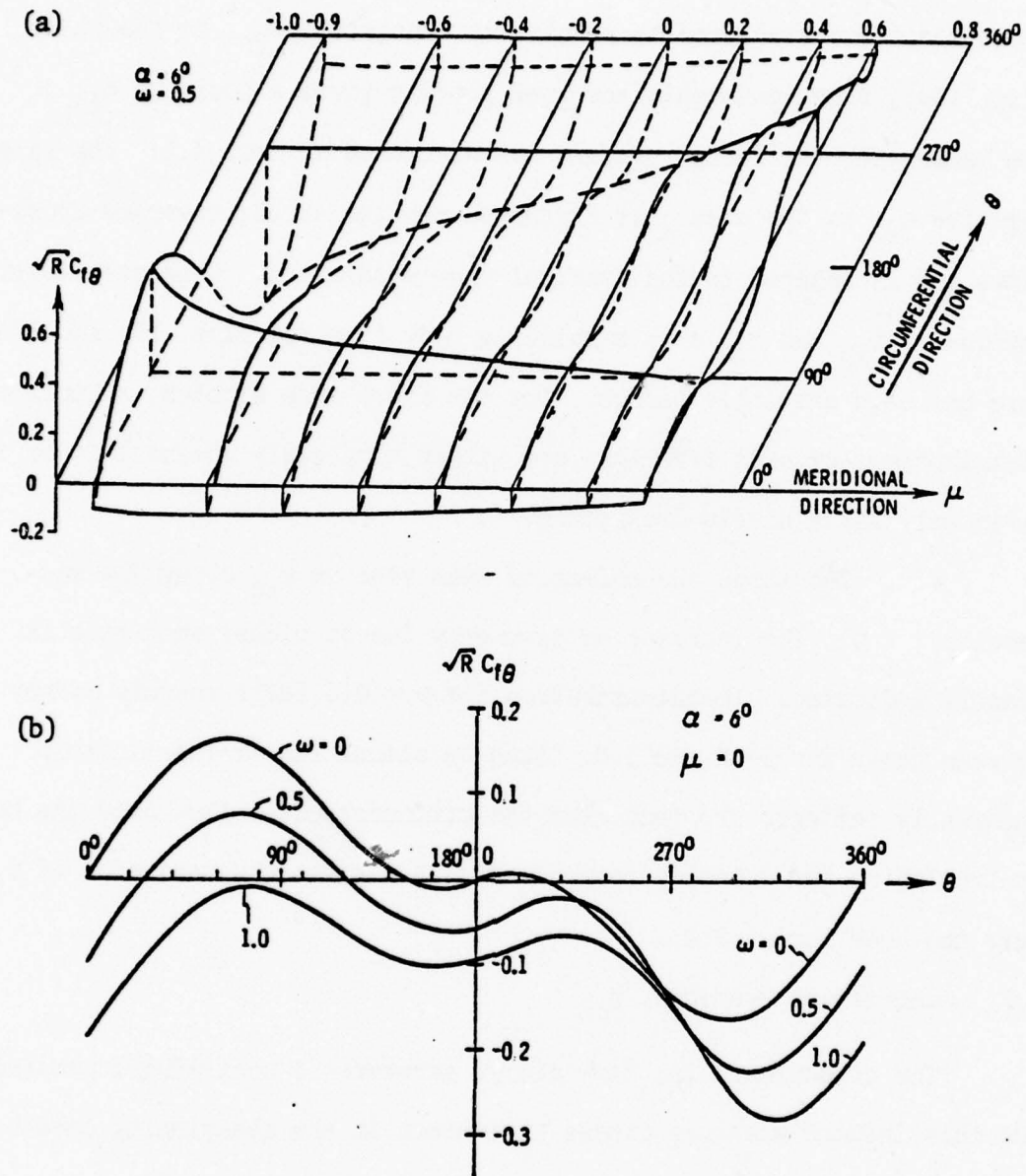


Fig. 2.0. Circumferential skin friction,  $c_{f\theta}$ . (a) Distribution of  $c_{f\theta}$ ,  $\omega = 0.5$ . (b) Comparison of  $c_{f\theta}$  for different  $\omega$ 's.

a monotonic reversed profile results in a negative  $c_{f\theta}$ , in the other (Fig. 13d), a non-monotonic reversed profile gives a positive  $c_{f\theta}$ . The reason for the latter profile was discussed in Sec. 4.2. The large positive  $c_{f\theta}$  in the area just discussed implies strong reversed cross-flows and is related to the eventual flow-separation. Complete distributions of  $c_{fu}$  and  $c_{f\theta}$  over a spinning body (such as Figs. 19a and 20a) have not been available before. For the sharp cone problem, calculated distributions of skin frictions are either completely absent<sup>(8,9)</sup> or given only for a single crossplane.

Fig. 20b shows the effect of spin rate on  $c_{f\theta}$  along the mid-section,  $\mu = 0$ . The increase of asymmetry due to higher spin rate is clearly indicated. The distribution for  $\omega = 0.5$  falls roughly midway between those for  $\omega = 0$  and 1.0. Such an almost linear relationship apparently reflects the fact that the circumferential flow near the body is controlled by the spinning motion. Fig. B-6 gives the variation of  $c_{f\theta}$  over the body for  $\omega = 1.0$ .

#### 4.7. Centrifugal Pressure, $p_{ct}$

The circumferential flow always generates a centrifugal pressure, but this induced pressure causes no concern in the nonspinning case because the contributions from the two sides of the symmetry-plane cancel each other. The asymmetry of the circumferential flow profiles (Sec. 4.2) due to the body's spinning leads to an asymmetrical distribution of the centrifugal pressure,  $p_{ct}$  as shown in Fig. 21a for  $\omega = 0.5$ . In the circumferential direction, the variation of  $|p_{ct}|$  follows roughly that of the inviscid  $v$ -velocity



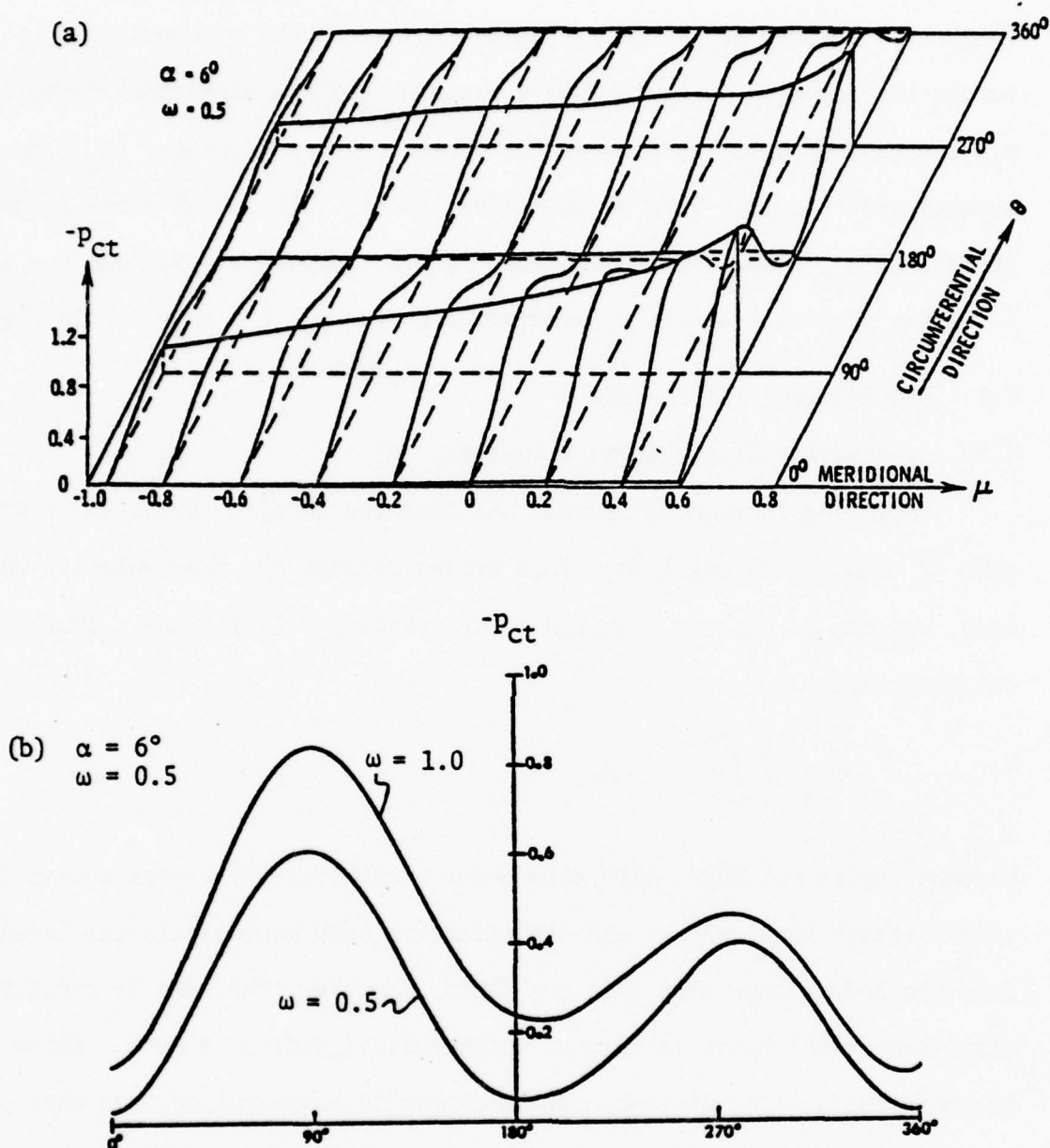


Fig. 21. Centrifugal pressure,  $p_{ct}$ . (a) Distribution of  $p_{ct}$ ,  $\omega = 0.5$ . (b) Comparison of  $p_{ct}$  for different  $\omega$ 's.

(Fig. 11); maximum  $|p_{ct}|$  occurs at  $\theta = 90^\circ$  where the  $v$ -velocity across the boundary layer reaches a maximum. In the meridional direction,  $p_{ct}$  increases toward the rear as the boundary layer thickens.  $|p_{ct}|$  increases with the spin rate as is evident in Fig. 21b, which shows a comparison of  $p_{ct}$  along the mid-section,  $\mu = 0$ , between  $\omega = 0.5$  and  $\omega = 1.0$ . A similar general trend of  $p_{ct}$ -distribution for  $\omega = 1.0$  is given in Fig. B7.

#### 4.8. Displacement Thicknesses

##### 4.8a. $v$ -Velocity Displacement Thickness, $\Delta_\theta^*$

Spinning introduced certain new features in  $\Delta_\theta^*$ . First it is noted that  $\Delta_\theta^*$  can become negative. This arises because the flow velocity on the body,  $v_B$ , can be greater than the outer velocity  $V$  (Fig. 22b). Thus the defining integral

$$V\Delta_\theta^* = \int_0^\infty (V-v)dz$$

becomes negative. Physically this means that viscosity causes a mass flow excess rather than defect, and the effective body boundary is displaced into the body rather than into the fluid. However, the idea of negative displacement thickness is only of conceptual significance here. Since the circumferential-flow displacement thickness is much smaller than that of the meridional-flow, the total displacement thickness is still positive.

Secondly the above integral becomes indeterminate when  $V$  vanishes. The latter happens at  $\theta = 0$  and  $\pi$ . In the nonspinning case, vanishing  $V$  leads to the vanishing of the  $v$ -profile across the boundary layer, so  $\Delta_\theta^*$  can be simply set to zero. In the spinning case, this is not true.  $q$  is chosen to replace  $V$  as the normalizing factor (see Eqs. 9a,b). The latter

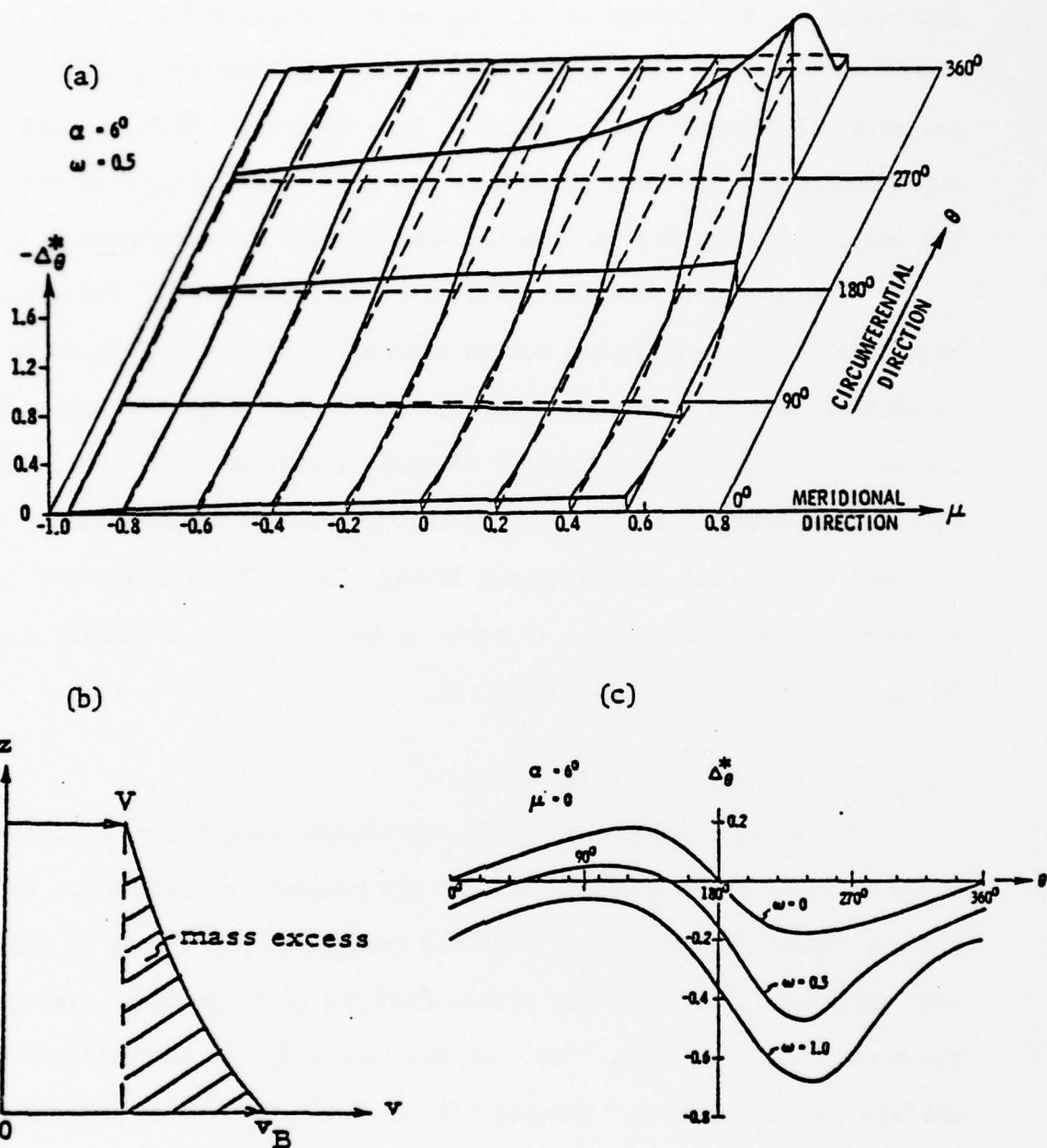


Fig. 22.  $v$ -velocity displacement thickness,  $\Delta_{\theta}^*$ .  
 (a) Distribution of  $\Delta_{\theta}^*$ . (b) Physically negative  $\Delta_{\theta}^*$ .  
 (c) Comparison of  $\Delta_{\theta}^*$  for different  $\omega$ 's.

introduces a complication in that  $\Delta_\theta^*$  becomes negative for  $\pi < \theta < 2\pi$  where  $V$  is negative. The negative  $\Delta_\theta^*$  discussed above for positive  $V$  has physical meaning; the negative  $\Delta^*$  here does not. This awkward situation could have been avoided if one added a minus sign in front of the integral in Eq. 9c; but then  $\Delta_\theta^*$  would become discontinuous at  $\theta = 180^\circ$ .

Fig. 22a gives the distribution of  $\Delta_\theta^*$  for  $\omega = 0.5$ . The maximum magnitude in the  $\theta$ -direction occurs around  $\theta = 270^\circ$ . This is to be expected physically because of strong reversed flow there. Fig. 22c compares  $\Delta_\theta^*$  for various spin rates at the mid-section,  $\mu = 0$ , with the higher spin rate ( $\omega = 1.0$ ) causing  $\Delta_\theta^*$  to be negative throughout. To be consistent,  $\Delta_\theta^*$  for the nonspinning case is considered in Fig. 22c to be negative for  $\pi \leq \theta \leq 2\pi$  although conventionally this is taken to be positive. A similar distribution of  $\Delta_\theta^*$  for  $\omega = 1.0$  is given in Fig. B8.

#### 4.8b. Total Displacement Thickness, $\Delta^*$

The total displacement  $\Delta^*$  is calculated using Eq. (11). Its distribution for  $\omega = 0.5$  is shown in Fig. 23a. At the present low incidence ( $\alpha = 6^\circ$ ), the meridional flow dominates over the crossflow, and the total displacement thickness  $\Delta^*$  differs very little from the corresponding  $u$ -velocity displacement thickness (Fig. 23b). At the fore-body,  $\Delta^*$  is small and nearly uniform around the body. Farther aft,  $\Delta^*$  increases and the maximum thickness position shifts from  $180^\circ$  into the direction of spinning, so that the displaced body is twisted longitudinally. Fig. 23a shows slight irregularities near  $\theta = 0^\circ$  and  $\theta = 180^\circ$  over the aft-body. This is a computational effect, but does not affect the rest of the results. The asymmetry of  $\Delta_\mu^*$  distribution again reflects the spinning effect on the longitudinal flow through its



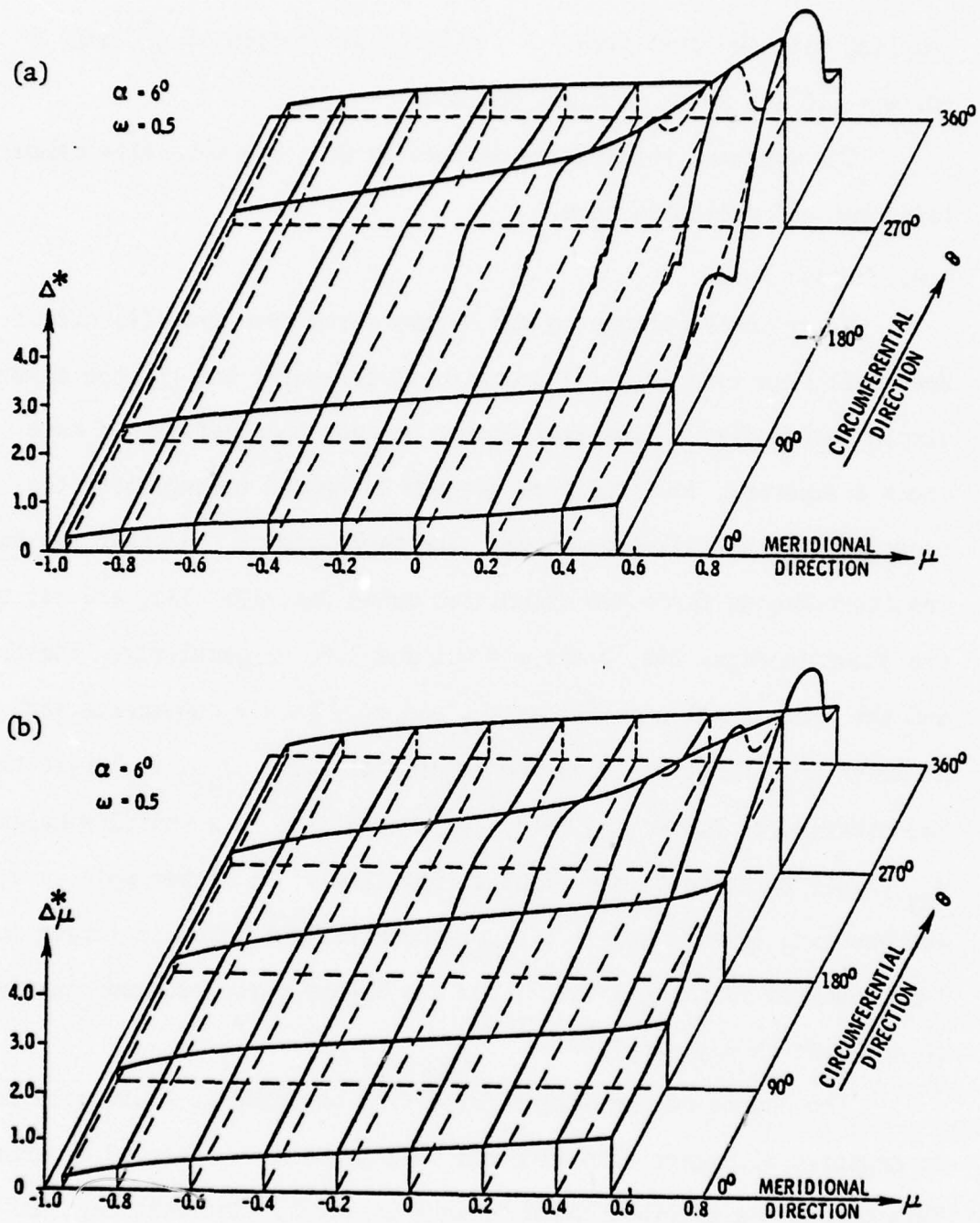


Fig. 23. (a) Total displacement thickness,  $\Delta^*$ ; (b) u-velocity displacement thickness,  $\Delta_\mu^*$ .

coupling with the crossflow. A similar distribution of  $\Delta_{\mu}^*$  and  $\Delta^*$  for  $\omega = 1.0$  are shown in Figs. B9, B10.

The momentum thicknesses defined by Eq. 10a-d were also calculated but not presented here.

#### 4.9. Magnus Force

Major contributions to the Magnus force come from (1) circumferential skin friction, (2) centrifugal pressure, and (3) the asymmetric displacement effect. The last factor has not been determined here because a separate, inviscid-flow program is needed to calculate the pressure over the displaced body. The magnitude of the other two and the resultant Magnus force are calculated using Eqs. 12b, 13c, and 14; the results are shown in Figs. 24a, b for  $\omega = 0.5$  and 1.0, respectively. The frictional and the centrifugal side-forces  $c_{sf}$  and  $c_{ct}$ , partly compensate each other. At lower spin rate,  $\omega = 0.5$ , the frictional force,  $c_{sf}$ , is larger than the centrifugal force,  $c_{ct}$  (Fig. 24a), resulting in a positive Magnus force,  $c_{mg}$  (i.e., pointing to the right in Fig. 24a). At higher spin rate,  $\omega = 1.0$ , the opposite is obtained--- i.e., the centrifugal force is larger in magnitude than the frictional force, and the Magnus force becomes negative (i.e., to the left in Fig. 24b).

The change of the Magnus force from positive at lower spin rate to negative at higher spin rate has been previously observed experimentally<sup>(26)</sup>. This change was ascribed there to wake vortices. Incidentally, Ref. 26 provides an extensive literature of experiments on the Magnus effect not mentioned in the present work. A series of flow-visualization pictures can be found in Ref. 27.

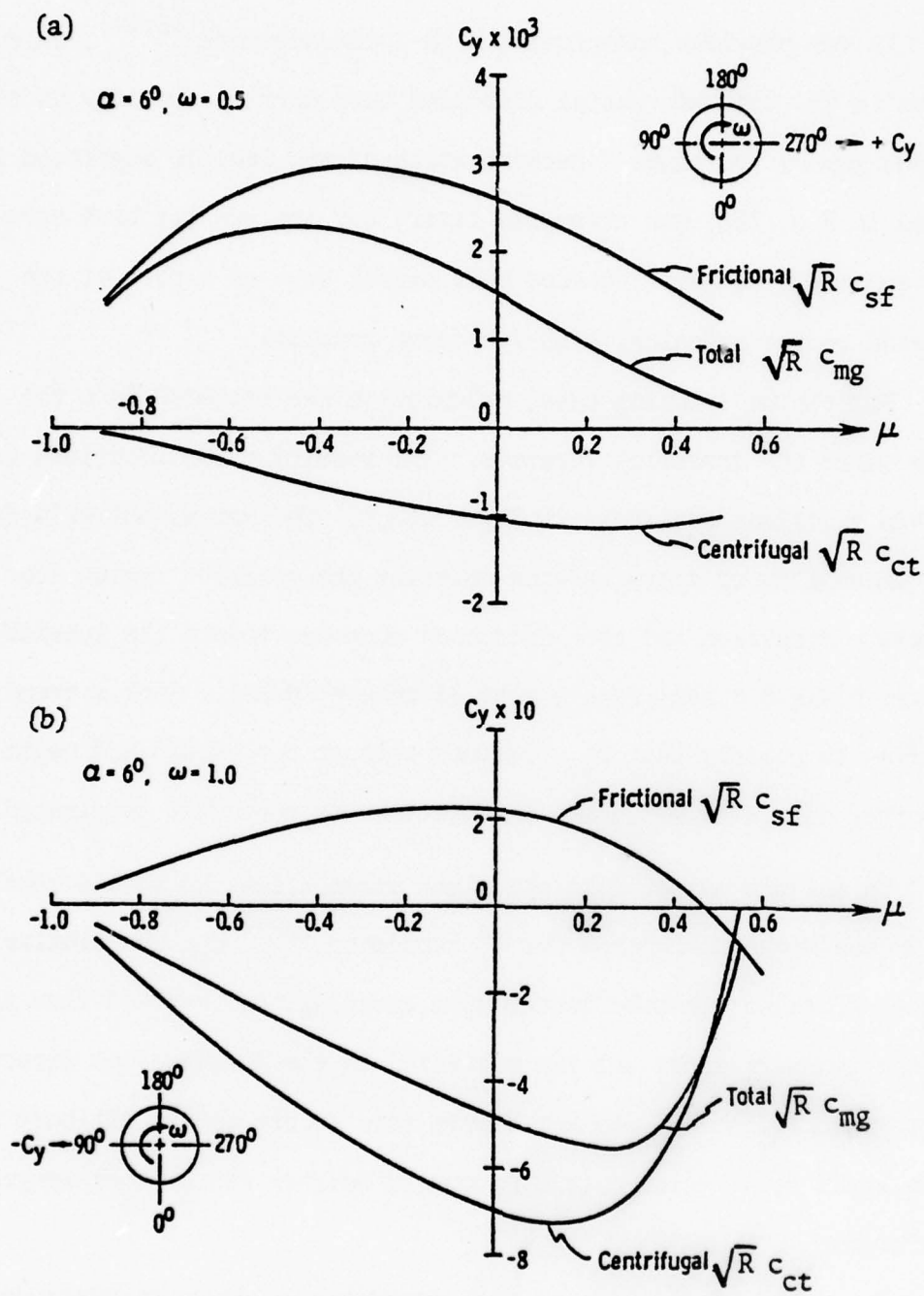


Fig. 24. Sectional side-force.

#### 4.10. The High-Incidence Problem

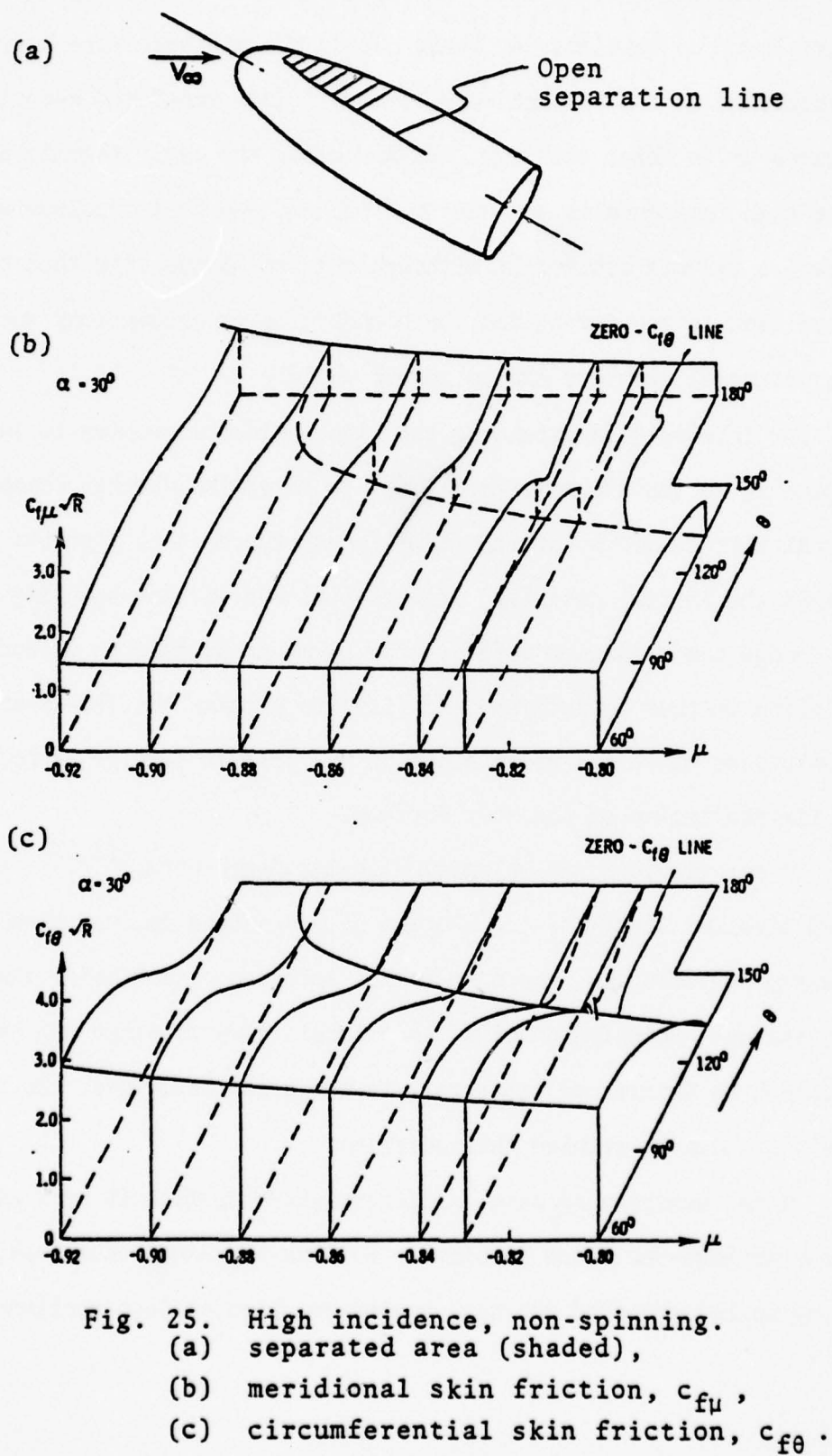
In our previous nonspinning high-incidence work<sup>(13,14)</sup>, calculations in the circumferential direction were carried out only up to the open separation lines. Determination of the leeside separated flow (shaded in Fig. 25a) was attempted later, but the results have never been reported. We have included that effort here as a part of the extension to the spinning, high-incidence problem.

For the nonspinning case, calculation was extended into the region where the crossflow reverses. The resulting distributions for the skin frictions are shown in Figs. 25b,c. The meridional skin friction  $c_{f\mu}$ , shows a sharp decrease upon entering the reversed region from the windward direction and then increases somewhat toward the leeside symmetry-plane  $\theta = 180^\circ$  (see  $\mu = -0.88$  to  $\mu = -0.86$ ). Such a trend intensifies so rapidly that  $c_{f\mu}$  becomes zero at  $\mu = -0.833$  and negative thereafter near  $\theta = 140^\circ$ . The calculation was therefore terminated.

To put the matter into the right prospective, we should recall that in the nonspinning case for  $6^\circ$  incidence,<sup>(12)</sup>  $c_{f\mu}$  was similarly found to decrease somewhat faster upon entering the reversed flow region from the windward side, but the variation in the longitudinal direction was so gradual that  $c_{f\mu}$  did not become zero except on the aft-body and the reversed flow region extending over a quarter of the body length was calculated.

The quick termination at high incidence leads us to conclude that the leeside separated region associated with an open-separation can not be determined according to the classical boundary layer theory. This is by no means an obvious conclusion from the outset, because it does not





seem to be certain that the flow involved violates in any way the boundary layer assumptions, at least not in the upstream fore-body. Our experience in the low incidence case<sup>(12)</sup> just mentioned especially encourages us to think this way. In any case, the early termination for the high incidence is somewhat unexpected, and it is unclear what the precise reasons are for it although one can always cite that the reversed flow is too strong and the boundary layer assumptions such as the potential pressure are no longer valid.

Our interests in extending the high incidence problem to include the spinning motion are multifold: (i) to determine whether boundary layer calculation can be started even though there is no rigorous way to obtain the initial profiles, (ii) to find out whether spinning motion would change the crossflow sufficiently so as to be able to extend the calculation further downstream, and (iii) to examine the flow features from solutions which can be obtained by the present simpler method, even for a limited region of the body surface.

In our previous non-spinning high-incidence work,<sup>(13,14)</sup> the problem involved first the calculation of stagnation region, then the symmetry-plane solution, the nose region solution, and finally the main-body solution. Spinning couples these local flows together and hence they cannot be determined separately in the order described. No rational way is now known to resolve this question.

In the nonspinning case, different starting methods were used for the low-and high-incidence problems. For the high-incidence case, the starting method employed the nose region solution as just mentioned. For

the low incidence case, approximate profiles were made up on the justification that the boundary layer varies only slightly from the windside toward the leeside over the fore-body.

For the spinning case, the starting profiles for low incidence ( $6^\circ$ ) were described in Sect. 3.4a. The question then is whether the same technique can be employed for the high-incidence case. When this was tried out, it was found (somewhat surprisingly) that calculation proceeded downstream without difficulty. The starting station was located at  $\mu = -0.943$ . This is not for any other reason than that the nonspinning solution for this particular  $\mu$ -station previously calculated was still available on tape. This nonspinning solution modified by a pure spinning profile (Fig. 8) makes up the required initial profiles.

Two spinning cases with  $\omega = 0.5$  and  $1.0$  are calculated for the same ellipsoid (Fig. 2) at  $30^\circ$  incidence. Sample results of the  $v$ -velocity profile are shown in Fig. 26 for  $\omega = 0.5$  at  $\mu = -0.836$ . More details of these profiles are given in Fig. B11.

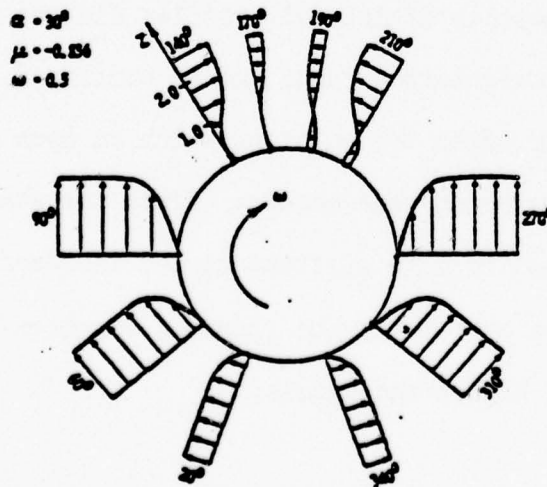


Fig. 26.  $v$ -velocity profiles for  $\alpha = 30^\circ$ ,  $\omega = 0.5$ .

The calculated meridional skin friction,  $c_{f\mu}$ , for  $\alpha = 30^\circ$  and  $\omega = 0.5$  is shown in Fig. 27a. Compared to Fig. 19 for  $6^\circ$  incidence, the  $c_{f\mu}$ -distribution along a fixed  $\mu$ -station changes noticeably within a short longitudinal distance (from  $\mu = -0.940$  to  $\mu = -0.833$  in Fig. 27a). Along  $\mu = -0.87$  or  $-0.85$ ,  $c_{f\mu}$  increases from  $\theta = 0^\circ$  to  $\theta = 90^\circ \sim 100^\circ$ , decreases sharply around  $\theta = 140^\circ \sim 160^\circ$ , then increases again slightly up to  $\theta = 220^\circ \sim 240^\circ$ . Around  $\theta = 250^\circ$ , a second dip appears. At  $\mu = -0.833$ ,  $c_{f\mu}$  drops almost to zero at  $\theta = 160^\circ$  so that the present calculation must be terminated. This occurs at the same  $\mu$ -station as for the nonspinning case. The corresponding distribution of  $c_{f\theta}$  is shown in Fig. 27b, which displays similar trends as Fig. 20a.

The skin frictions for  $\omega = 1.0$ ,  $\alpha = 30^\circ$  are given in Fig. B-12. Increase of the spin rate enables the calculation to be extended downstream slightly (terminated at  $\mu = -0.812$ ), but otherwise the same characteristics prevail.

Thus the question of initial profiles did not present an unsurmountable problem, but calculation could not be continued in the longitudinal direction very far after the point at which an open separation for the corresponding nonspinning case occurs. Since the starting point of open separation continues to move upstream as the incidence increases<sup>(28)</sup>, this means that the area over which the spinning boundary layer can be calculated decreases at higher incidences.



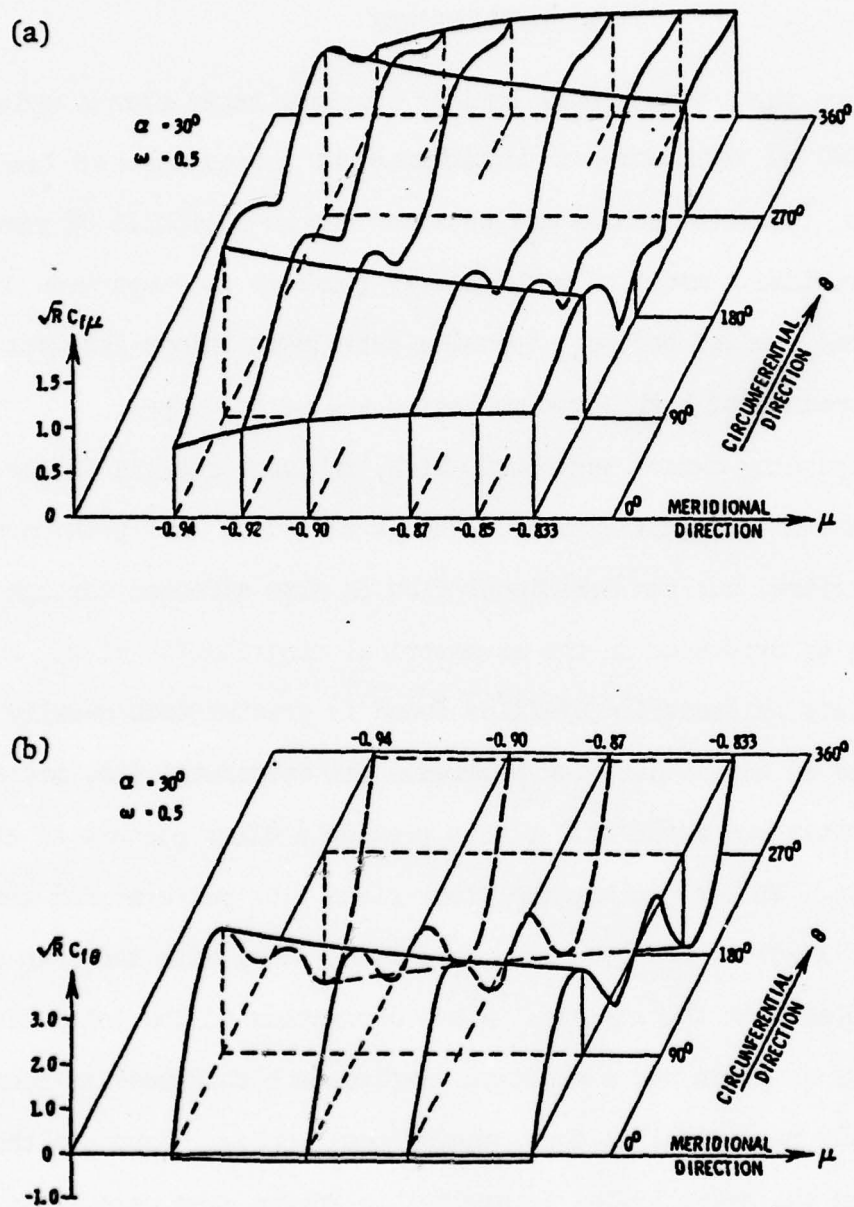


Fig. 27. Skin friction distribution. (a)  $c_{f\mu}$  and  
(b)  $c_{f\theta}$ .

## 5. CONCLUSIONS

The three-dimensional laminar boundary layer over a spinning blunt body of revolution at incidence is investigated here. Complete, concrete results are obtained for an ellipsoid of revolution which provides a model of more general geometry in comparison with the sharp cone studied before. Spinning introduces unique features from the viewpoints of both fluid mechanics and methodology.

Spinning causes asymmetry which, in turn, results in the side forces known as Magnus effects. The asymmetry is most pronounced in the crossflow, but the meridional flow is also affected through the coupling as evidenced in the asymmetrical distribution of  $c_{f\mu}$  and  $\Delta_\mu^*$ . The variety of crossflow profiles found is greater than usually encountered in any single flow problem. The calculated flow patterns in the cross-and meridional-planes provide a clear picture of the flow structure. In particular, the cross-plane flow patterns and the singularities involved are presented in detail, along with the skin frictions and displacement thicknesses. A new derivation of the total displacement thickness is given and a negative displacement thickness is found to be physically meaningful in the spinning-body boundary layer, although its effect on the overall flow is negligible in the case calculated. The Magnus forces due to the circumferential skin friction and the centrifugal pressure are determined; these two forces partly compensate each other. At lower spin rates, the frictional force is larger, resulting in a positive Magnus force. At higher spin rates, the opposite is the case. The overall magnitude of the Magnus force increases with spin rate.

At high incidence ( $30^\circ$ ), boundary layer calculations are carried out in the longitudinal direction only up to where an open separation occurs. The leeside separated region associated with an open separation is not amenable to a classical boundary layer treatment. It is not certain whether this difficulty can be overcome merely by using an experimental pressure distribution instead of the potential-flow pressure used here.

Methodologically, the present work strictly follows the boundary layer theory, which does not become invalid merely because of the presence of the crossflow reversal. The associated zone of dependence can be effectively observed with the Krause scheme. The generation of initial profiles to start the calculation did not lead to an impasse as previously conceived. Profiles for the longitudinal march can be approximated by superimposing the corresponding nonspinning profile with an assumed pure spinning profile. Those for the circumferential march are generated as the computation proceeds. The present calculation terminates when the meridional skin friction,  $c_{f\mu}$ , becomes zero because the boundary layer theory ceases to be valid when both the  $u$ - and the  $v$ -profiles reverse. In this respect, the parabolicized approach offers no advantage. To save computing time, experiments were made to show that larger step-sizes can be used, depending on how severe the relevant adverse pressure gradient is. The case of  $\omega = 1.0$  at  $6^\circ$  incidence was calculated with less than one hour of CPU time on a UNIVAC 1108 computer.

## ACKNOWLEDGEMENT

This work was sponsored by the U. S. Army Research Office under Contract No. DAHC04-73-C-0011. Subsequent extension of the work and the preparation of this report were supported by the U. S. Air Force Office of Scientific Research under Contract F49620-76-C-0004. The author is greatly indebted to Susan Yamamura and Richard Showers for their successive assistance in developing the computer program and obtaining the results.



## 6. REFERENCES

1. Prandtl, L., The Essentials of Fluid Dynamics. Blackie and Son Limited, London. 1952.
2. Martin, J. C., "On Magnus Effects caused by the Boundary-Layer Displacement Thickness on Bodies of Revolution at Small Angles of Attack,": J. Aero. Sci.. Vol. 24, pp. 421-429, June 1957.
3. Kelley, H. R., "An Analytical Method for Predicting the Magnus Forces and Moments on Spinning Projectiles," Naval Ord. Test Station TM-1634, Aug. 1954 (Not available).
4. Sedney, R., "Laminar Boundary Layer on a Spinning Cone at Small Angles of Attack in a Supersonic Flow," J. Aero. Sci., Vol. 24, pp. 430-436, June 1957.
5. Dwyer, H. A., "Hypersonic Boundary Layer Studies on a Spinning Sharp Cone at Angle of Attack," AIAA Paper No. 71-57, Jan. 1971.
6. Clark, B. L., "Navier Stokes Solutions for Laminar Incompressible Flow over Yawed Spinning Bodies of Revolution," AIAA Paper No. 72-112, Jan. 1972.
7. Vaughn, H. R. and Reis, G. E., "A Magnus Theory," AIAA Paper No. 73-124, Jan. 1973. (Not available).
8. Watkins, C. B., Jr., "Numerical Solution of the Three-Dimensional Boundary Layer on a Spinning Sharp Body at Angle of Attack," Computers & Fluids, Vol. 1, No. 4, pp. 317-329, 1973.
9. Lin, T. C. and Rubin, S. G., "Viscous Flow over Spinning Cones at Angle of Attack," AIAA Journal, Vol. 12, No. 7, pp. 975-985, July 1974.
10. Dwyer, H. A. and Sanders, B. R., "Magnus Forces on Spinning Supersonic Cones - Part I: The Boundary Layer," AIAA Journal, Vol. 14, No. 4, pp. 498-504, 1976.
11. Sanders, B. R. and Dwyer, H. A., "Magnus Forces on Spinning Supersonic Cones, Part II: Inviscid Flow," AIAA Journal, Vol. 14, No. 5, pp. 576-582, 1976.
12. Wang, K. C., "Boundary Layer over a Blunt Body at Low Incidence with Circumferential Reversed Flow," J. Fluid Mech., Vol. 72, Part 1, pp. 49-65, 1975.
13. Wang, K. C., "Boundary Layer over a Blunt Body at High Incidence with an Open-Type Separation," Proc. Royal Soc. London, A. 340, pp. 33-55, 1974.

14. Wang, K. C., "Boundary Layer over a Blunt Body at Extremely High Incidence," *Phys. of Fluids*, Vol. 17, No. 7, pp. 1381-1385, 1974.
15. Moore, F. K., "Displacement Effect of a Three-Dimensional Boundary Layer," *NACA TR 1124*, 1953.
16. Lighthill, M. J., "On Displacement Thickness," *J. Fluid Mech.*, Vol. 4, Part 4, pp. 383-392, 1958.
17. Wang, K. C., "Numerical Solution of Three-Dimensional Boundary Layer Equations," *MML TR 76-14C*, Feb. 1976.
18. Lamb, H., *Hydrodynamics*, pp. 141-142, 6th Edition, Dover, New York.
19. Dwyer, H. A., "Solution of a Three-Dimensional Boundary-Layer Flow with Separation," *AIAA Journal*, Vol. 6, No. 7, pp. 1336-1342, 1968.
20. Hall, M. G., "A Numerical Method for Calculating Steady Three-Dimensional Laminar Boundary Layers," *RAE TR 6714*, July 1967.
21. Krause, E., "Comment on Solution of a Three-Dimensional Boundary Layer Flow with Separation," *AIAA Journal*, Vol. 7, No. 3, pp. 575-576, 1969.
22. Watkins, C. B., "Laminar Symmetry Plane Boundary Layer on a Sharp Spinning Body at Incidence," *AIAA J.* Vol. 11, pp. 559-561, 1973.
23. Kitchens, C. W. Jr., Gerber, N. and Sedney, R., "Computational Implications of the Zone of Dependence Concept for Three-Dimensional Boundary Layers on a Spinning Body," *BRL Report No. 1774*, April 1975.
24. Richtmyer, R. D. and Morton, K. W., *Difference Methods for Initial-Value Problems*, Interscience Publishers, Wiley 1967.
25. Sears, W. R. and Telionis, D. P., "Boundary-Layer Separation in Unsteady Flow," *SIAM J. Applied Math.* Vol. 28, No. 1, pp. 215-235, Jan. 1975.
26. Jacobson, I. D., "Magnus Characteristics of Arbitrary Rotating Bodies," *AGARDograph No. 171*, 1975.
27. Werle, H., "Ecoulement a basse vitesse autour d'un fuselage anime d'un mouvement de rotation uniforme autout de son axe." *ONERA document No. 71/1859A*, Feb. 1966.
28. Wang, K. C., "Separation of Three-Dimensional Flow," *Proc. of the Viscous Flow Symposium*, Lockheed-Georgia Company, Atlanta, Ga., LG77ER0044, pp. 341-414, 1976. Also Martin Marietta Labs. TR-76-54C, August 1976.

## APPENDIX A

Derivation of the Equation Determining the Total  
Displacement Thickness for Three-Dimensional  
Boundary Layer

Consider a boundary layer volume element with the base area ( $h_x \Delta x$ ,  $h_y \Delta y$ ) as shown in Fig. A1.  $x$  and  $y$  are not necessarily the Cartesian coordinates,  $h_x$  and  $h_y$  are the corresponding metric coefficients. First, we

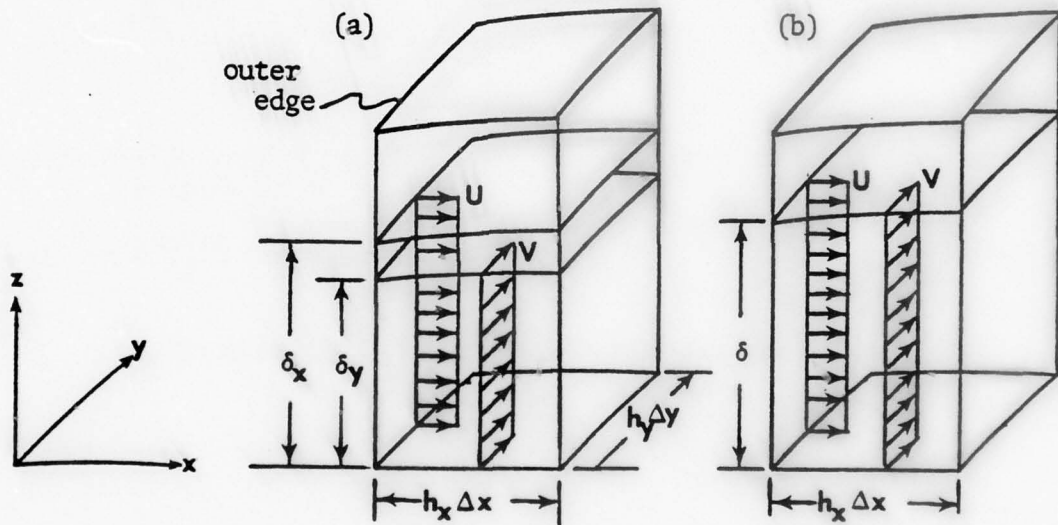


Fig. A1. Displacement thicknesses. (a)  $\delta_x$  and  $\delta_y$  for the component flows. (b) Total displacement thickness  $\delta$ .

define, as usual, two displacement thicknesses  $\delta_x$  and  $\delta_y$  (Fig. A1(a)) respectively for the  $x$ - and  $y$ - directions of flow with inviscid outer-edge velocities  $U$  and  $V$ ,

$$\begin{aligned}\delta_x &= \frac{1}{U} \int_0^\infty (U - u) dz \\ \delta_y &= \frac{1}{V} \int_0^\infty (V - v) dz\end{aligned}\tag{A-1}$$

In analogy with the usual reasoning in deriving the mass continuity equation, we consider

Incoming mass defect across the left surface

$$= U \delta_x h_y \Delta y$$

Incoming mass defect across front surface

$$= V \delta_y h_x \Delta x$$

Outgoing mass defect across the right surface

$$= \left( U \delta_x h_y + \frac{\partial U \delta_x h_y}{\partial x} \Delta x \right) \Delta y$$

Outgoing mass defect across the back surface

$$= \left( V \delta_y h_x + \frac{\partial V \delta_y h_x}{\partial y} \Delta y \right) \Delta x$$

Net change of the mass defect across the side-surfaces

$$= \frac{\partial U \delta_x h_y}{\partial x} + \frac{\partial V \delta_y h_x}{\partial y} \tag{A-2}$$

which is, of course, balanced by the mass flow across the top surface of the volume element, but this is not of our concern here.

Next we consider the mass defect of the same volume element in terms of a single displacement thickness  $\delta$  (Fig. A1(b)) which has no simple integral definition as Eq. (A-1) for  $\delta_x$  and  $\delta_y$ .  $\delta$  is so defined that the net mass defect across the side-surfaces for the same volume element in terms of  $\delta$  will be the same as Eq. (A-2) in terms  $\delta_x$  and  $\delta_y$ . The latter



condition is required in order to ensure the mass continuity upon replacing  $\delta_x$  and  $\delta_y$  by  $\delta$ , while the mass flow condition at the top surface is kept unchanged.

Following the same steps by comparing the outgoing and the incoming mass defects, we obtain the net change of mass defect across the side-surfaces in terms of  $\delta$

$$= \frac{\partial U \delta h_y}{\partial x} + \frac{\partial V \delta h_x}{\partial y} . \quad (A3)$$

Equating Eq. (A-3) to Eq. (A-2) yields

$$\frac{\partial U \delta_x h_y}{\partial x} + \frac{\partial V \delta_y h_x}{\partial y} = \frac{\partial U \delta h_y}{\partial x} + \frac{\partial V \delta h_x}{\partial y} ,$$

or

$$\frac{\partial}{\partial x} [h_y U (\delta - \delta_x)] + \frac{\partial}{\partial y} [h_x V (\delta - \delta_y)] = 0 , \quad (A4)$$

which is the equation first derived by Moore.<sup>(15)</sup> To specialize this equation to the streamline coordinates, we may set

$$V \equiv 0, \quad \frac{\partial V}{\partial x} = \frac{\partial V}{\partial y} = 0$$

and redefine

$$\delta_y = \frac{1}{U} \int_0^\infty v dz .$$

Then Eq. (A-4) becomes

$$\frac{\partial}{\partial x} [h_y U (\delta - \delta_x)] + \frac{\partial}{\partial y} (h_x U \delta_y) = 0 .$$

Integrating

$$h_y U (\delta - \delta_x) \Big|_0^x + \int_0^x \frac{\partial}{\partial y} (h_x U \delta_y) dx = 0. \quad (A-5)$$

Assume that  $x = 0$  is the stagnation point where the streamline originates and  $U = 0$ . Also in a streamline coordinate,  $h_x = \frac{1}{U}$ , hence Eq.(A-5) becomes

$$\delta = \delta_x - \frac{1}{h_y U} \int_0^x \frac{\partial \delta_y}{\partial y} dx, \quad (A-6)$$

which is the form given by Lighthill.<sup>(16)</sup> Lighthill derived Eq. (A-6) by four different methods, and refers to Moore's derivation as the method of velocity comparison. Our derivation follows the reasoning employed for the mass continuity equation, and is somewhat akin to Lighthill's flow reduction method, but differs in the formalism. Lighthill's derivation is also specialized to the streamline coordinates. It is straightforward to include the compressibility effect in Eq. (A-4) or to write it in slight by different form as Eq. (11) of the text.

## APPENDIX B

## Additional Figures

This appendix contains a number of additional figures obtained from this investigation.

- Fig. B1. v-velocity profiles,  $\alpha = 6^\circ$ ,  $\omega = 0.5$  and  $1.0$ .
- Fig. B2. Cross-plane flow pattern (rectangular),  $\alpha = 6^\circ$ ,  $\omega = 0.5$  and  $1.0$ .
- Fig. B3. Cross-plane flow pattern (circular),  $\alpha = 6^\circ$ ,  $\omega = 0.5$  and  $1.0$ .
- Fig. B4. Meridional-plane flow pattern,  $\alpha = 6^\circ$ ,  $\omega = 0.5$ .
- Fig. B5. Meridional skin friction,  $\alpha = 6^\circ$ ,  $\omega = 1.0$ .
- Fig. B6. Circumferential skin friction,  $\alpha = 6^\circ$ ,  $\omega = 1.0$ .
- Fig. B7. Centrifugal pressure,  $\alpha = 6^\circ$ ,  $\omega = 1.0$ .
- Fig. B8. v-velocity displacement thickness,  $\alpha = 6^\circ$ ,  $\omega = 1.0$ .
- Fig. B9. u-velocity displacement thickness,  $\alpha = 6^\circ$ ,  $\omega = 1.0$ .
- Fig. B10. Total displacement thickness,  $\alpha = 6^\circ$ ,  $\omega = 1.0$ .
- Fig. B11. v-velocity profiles,  $\alpha = 3.0^\circ$ ,  $\omega = 0.5$ .
- Fig. B12. Skin frictions for  $\alpha = 30^\circ$ ,  $\omega = 1.0$   
(a)  $c_{f\mu}$ , (b)  $c_{f\theta}$ .

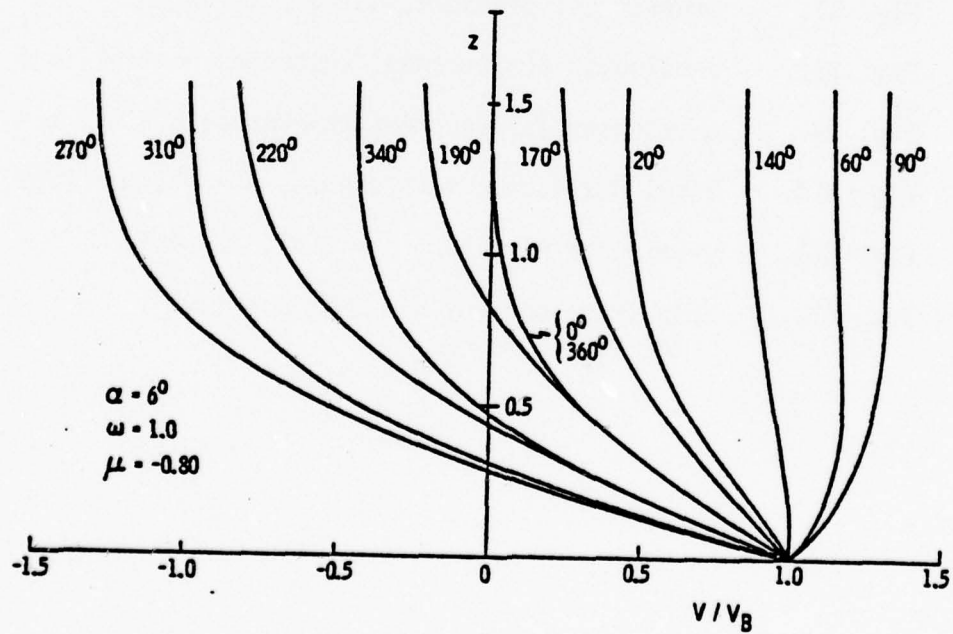
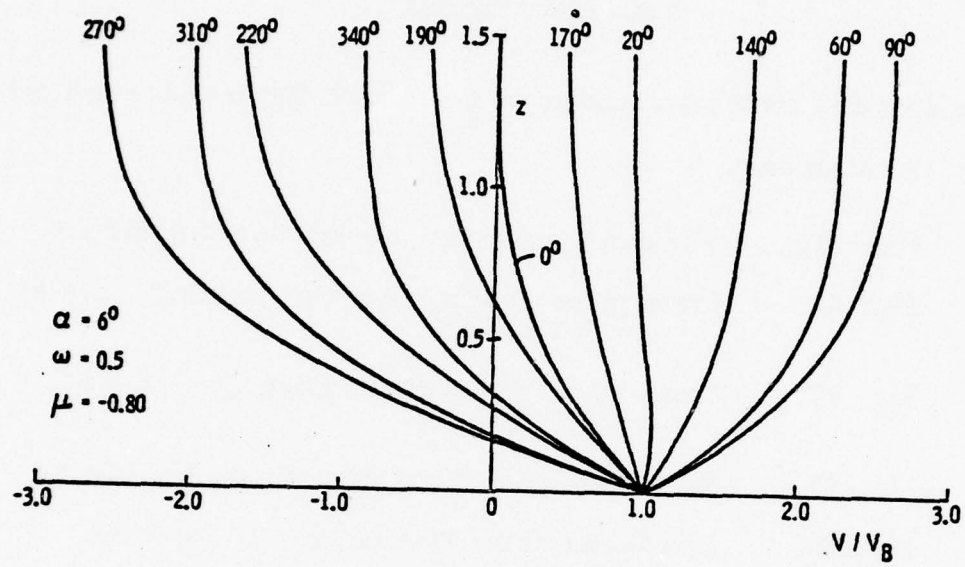
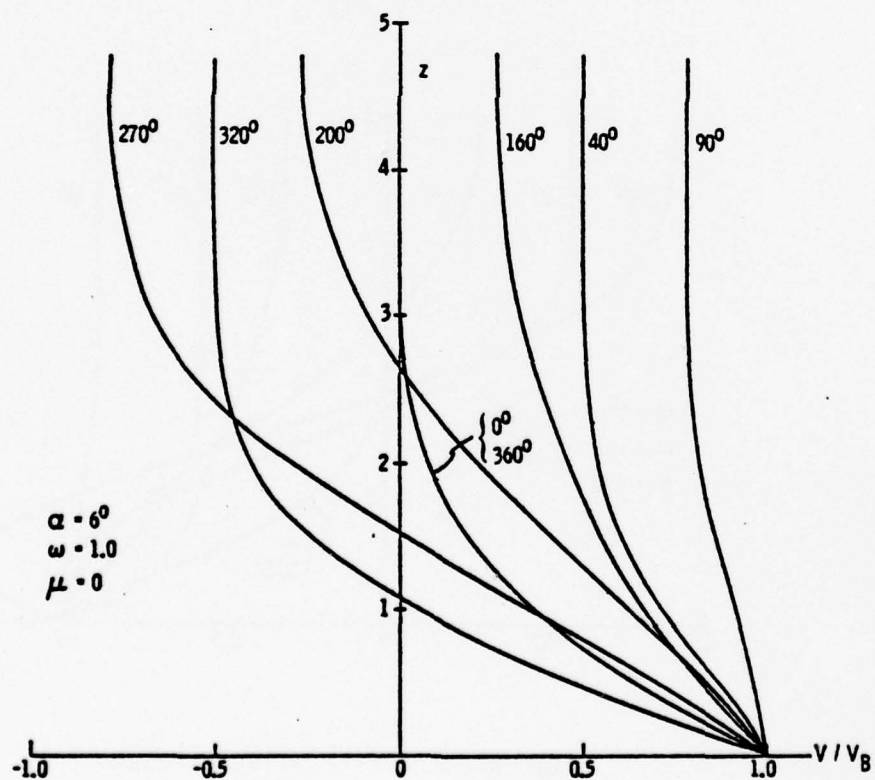
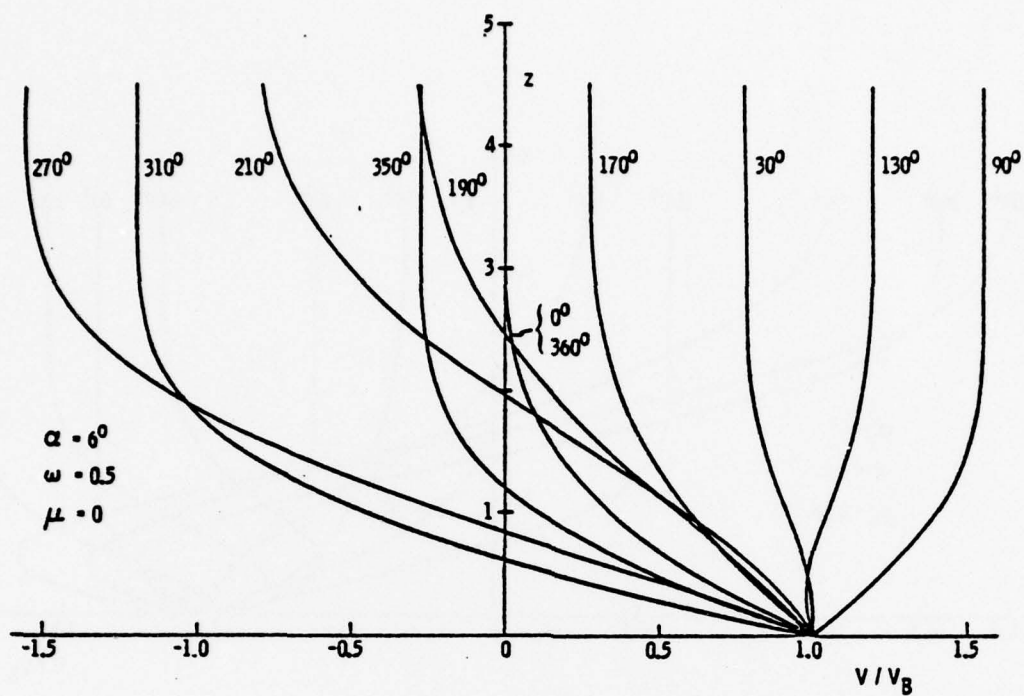


Fig. B1(a).  $v$ -velocity profile.



Fig. B1(b).  $v$ -velocity profile.

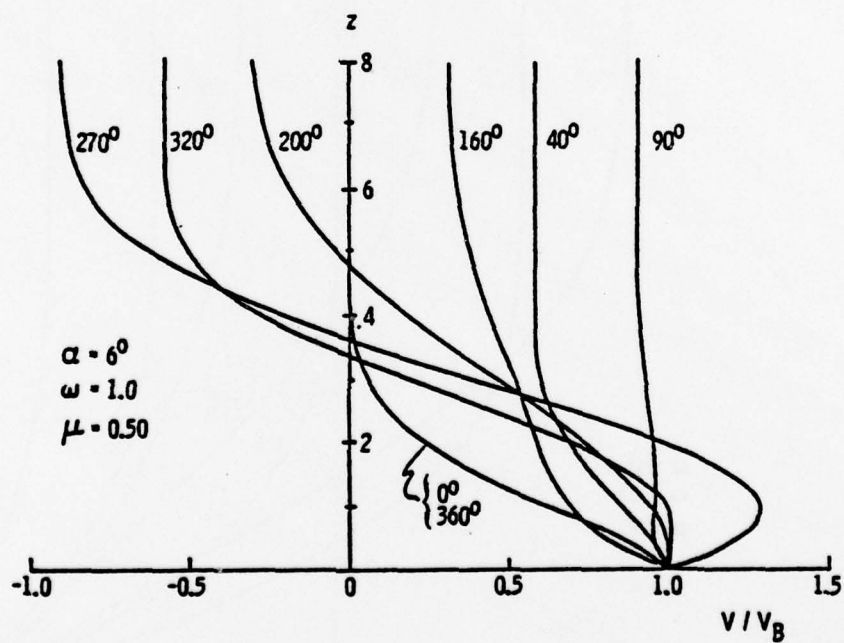
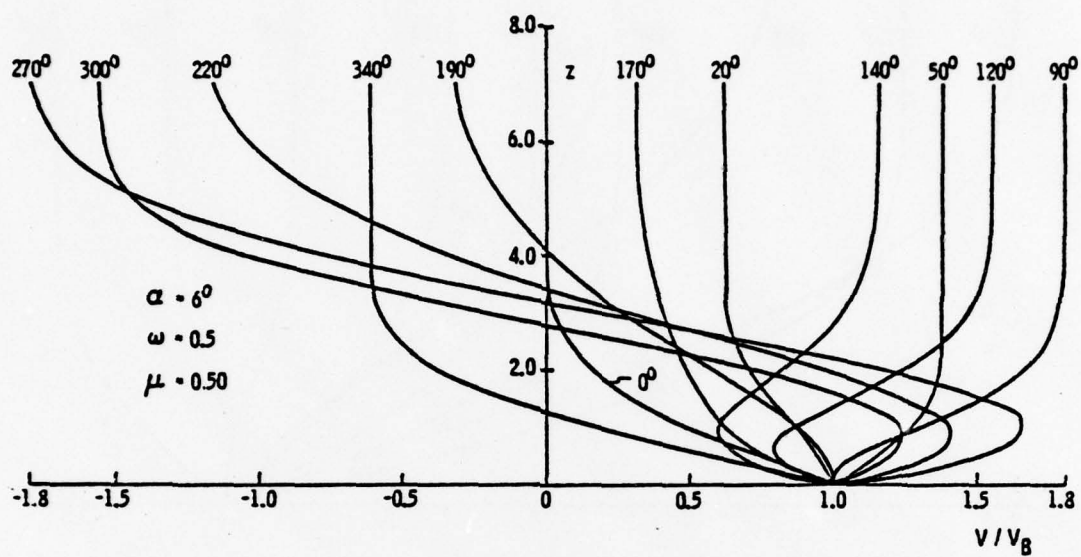


Fig. B1(c). v-velocity profile.

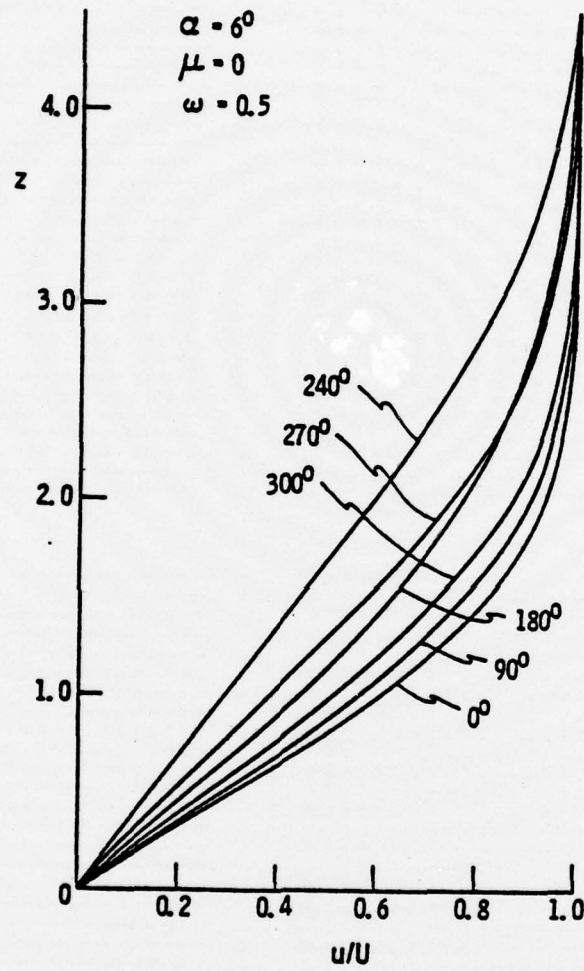


Fig. B1(d).  $u$ -velocity profile.

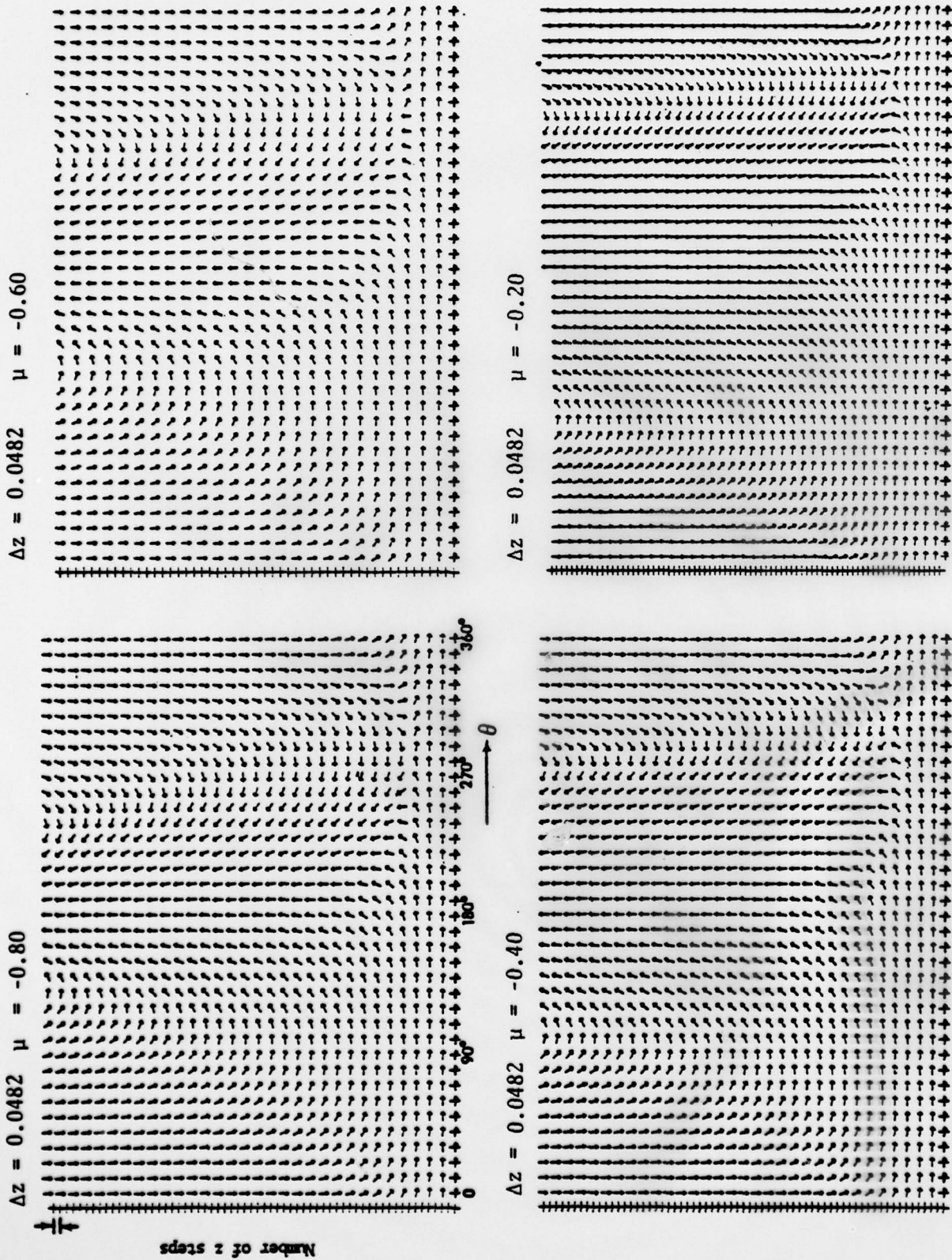
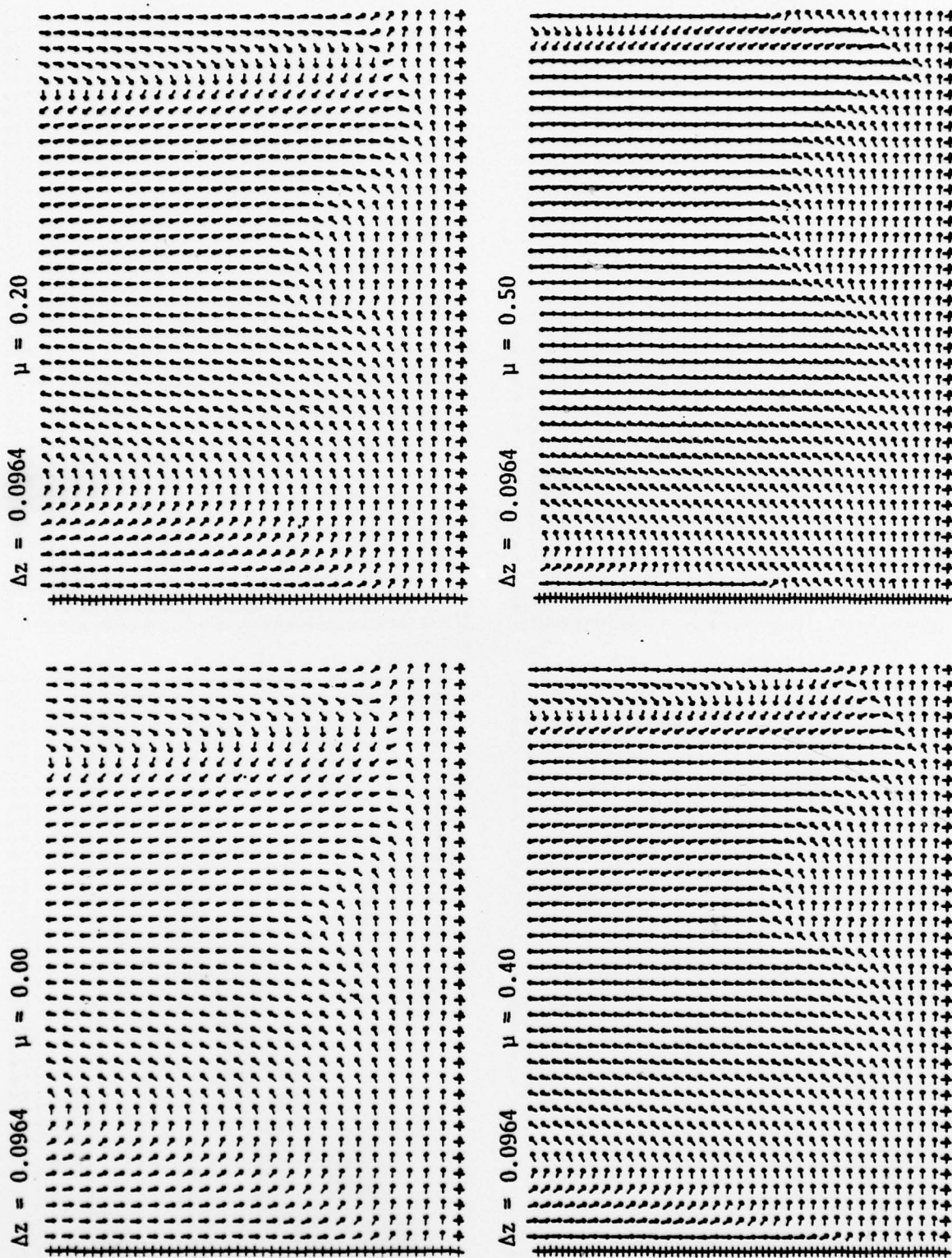


Fig. B2. Crossplane flow pattern (rectangular),  $\alpha = 6^\circ$ ,  $\omega = 0.5$ .



Fig. B2. Continued,  $\alpha = 6^\circ$ ,  $\omega = 0.5$

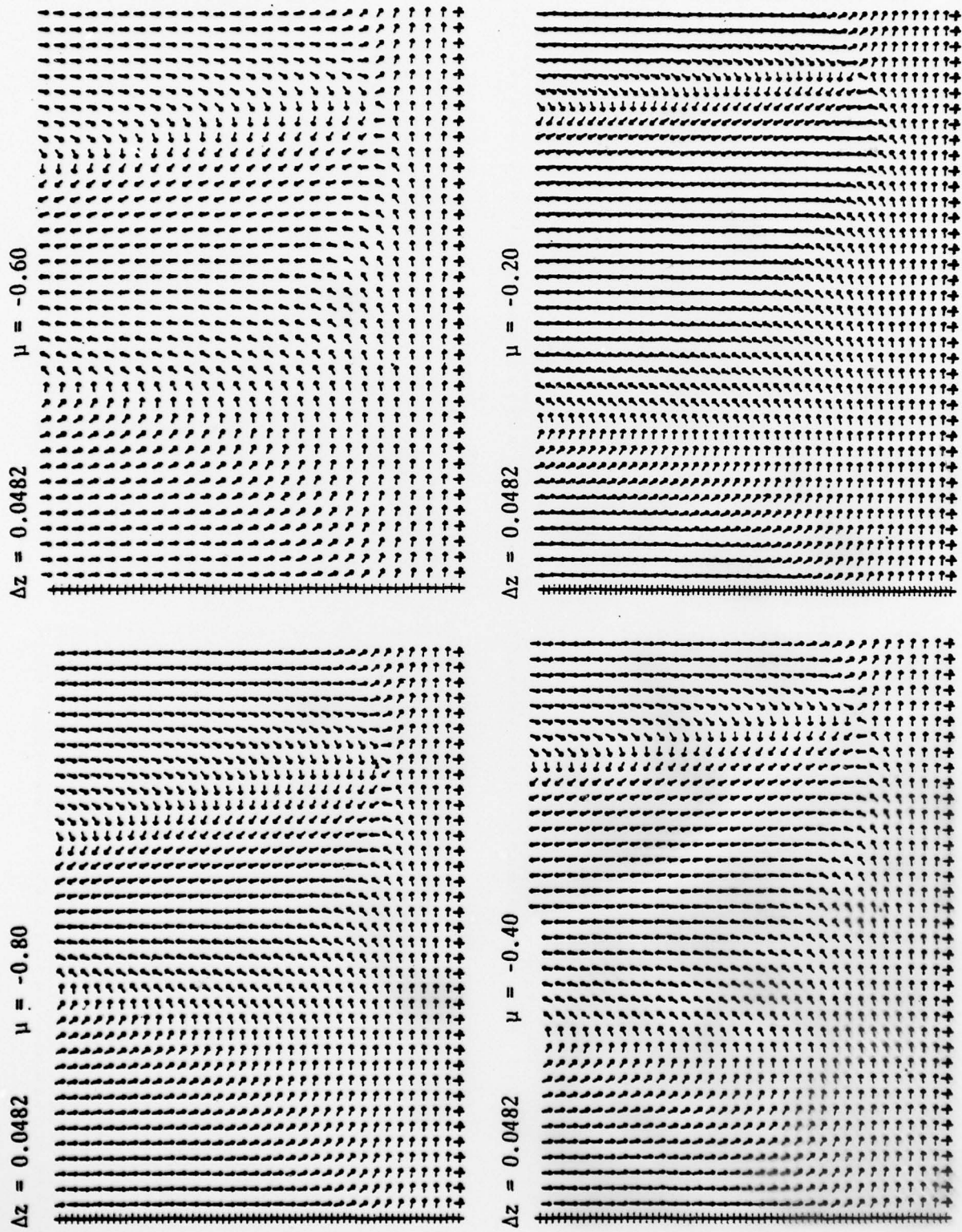
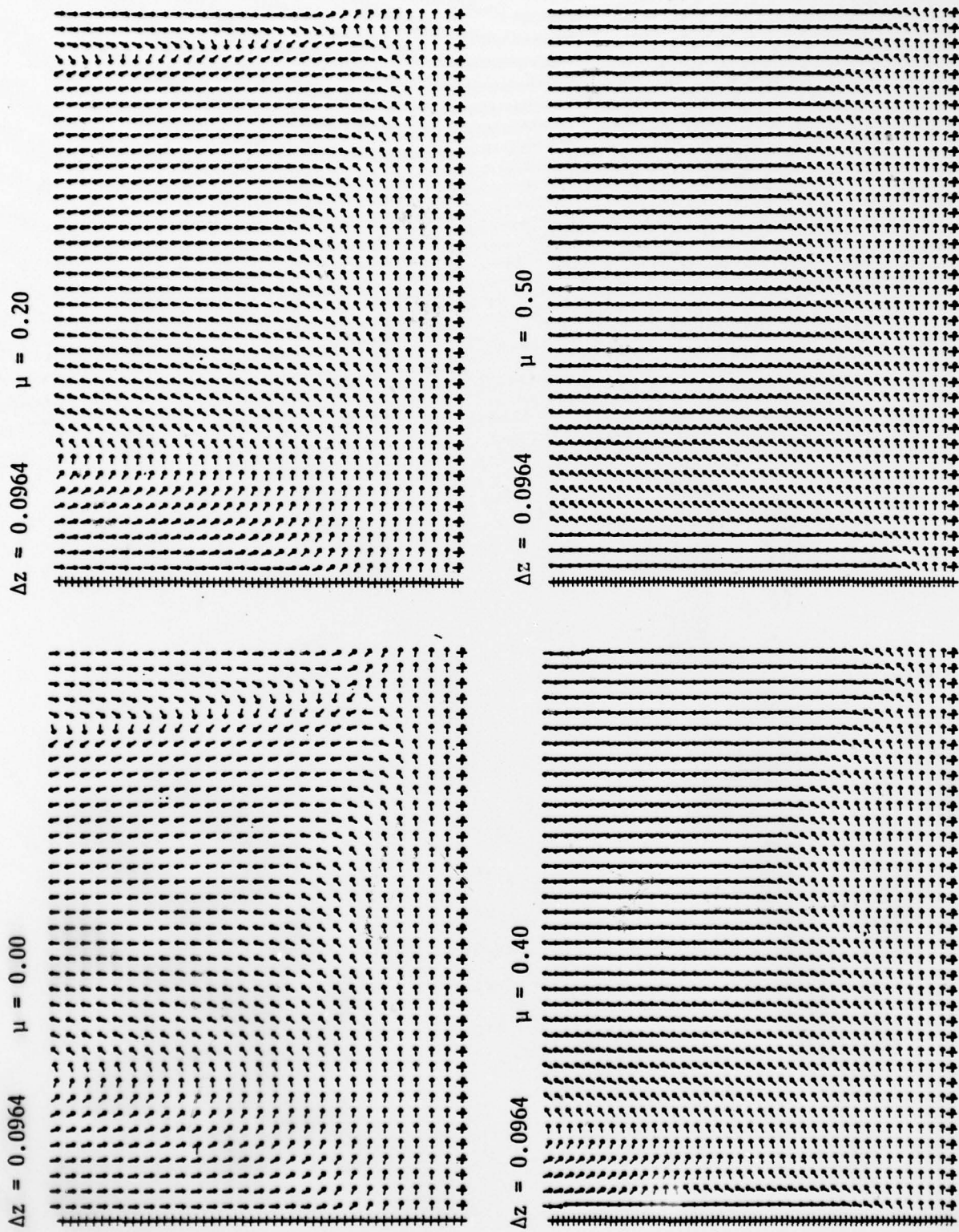


Fig. B2. Crossplane flow pattern (rectangular),  $\alpha = 6^\circ$ ,  $\omega = 1.0$ .



Fig. B2. Continued,  $\alpha = 6^\circ$ ,  $\omega = 1.0$ .

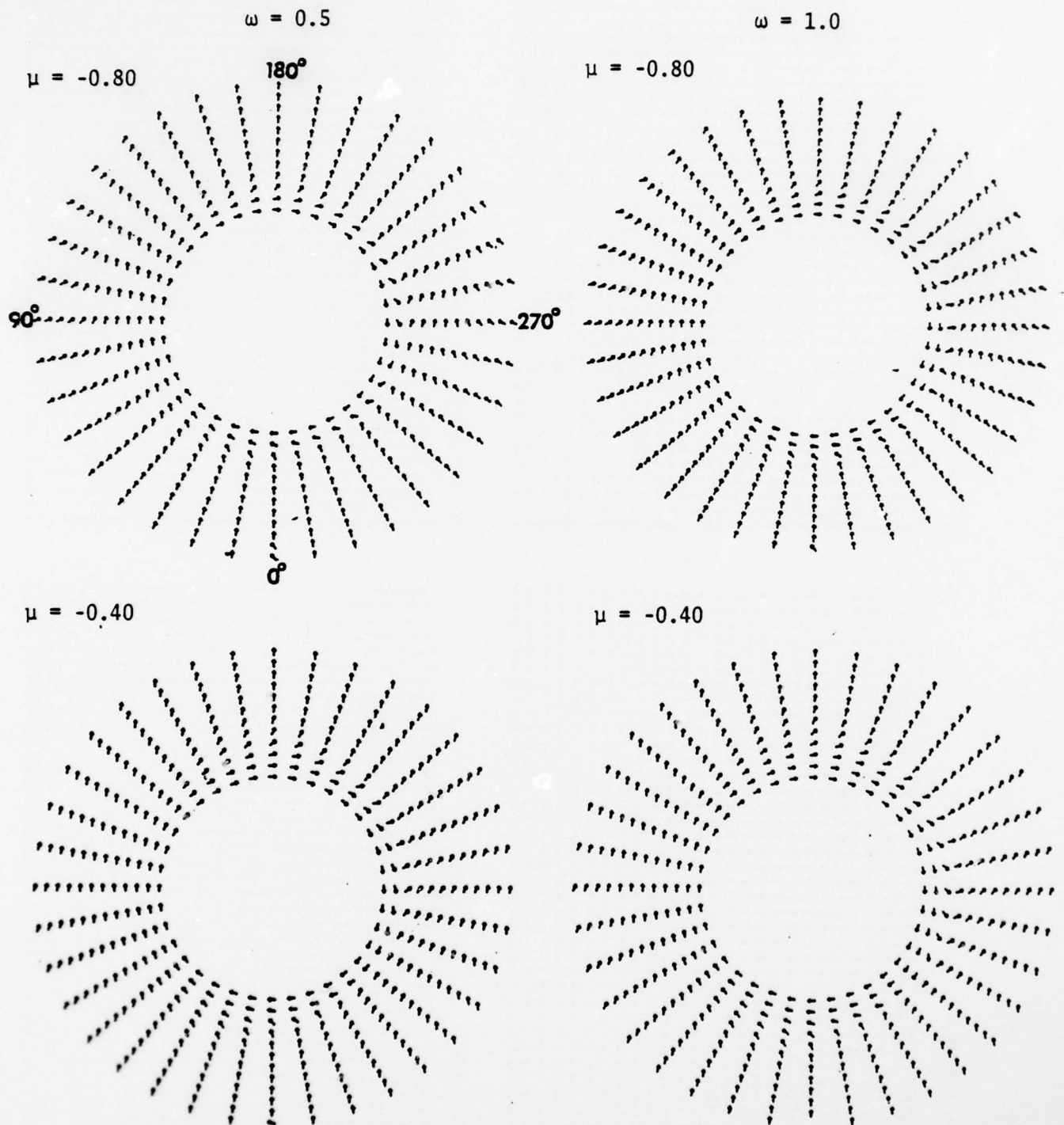


Fig. B3. Crossplane flow pattern (circular),  $\alpha = 6^\circ$ .



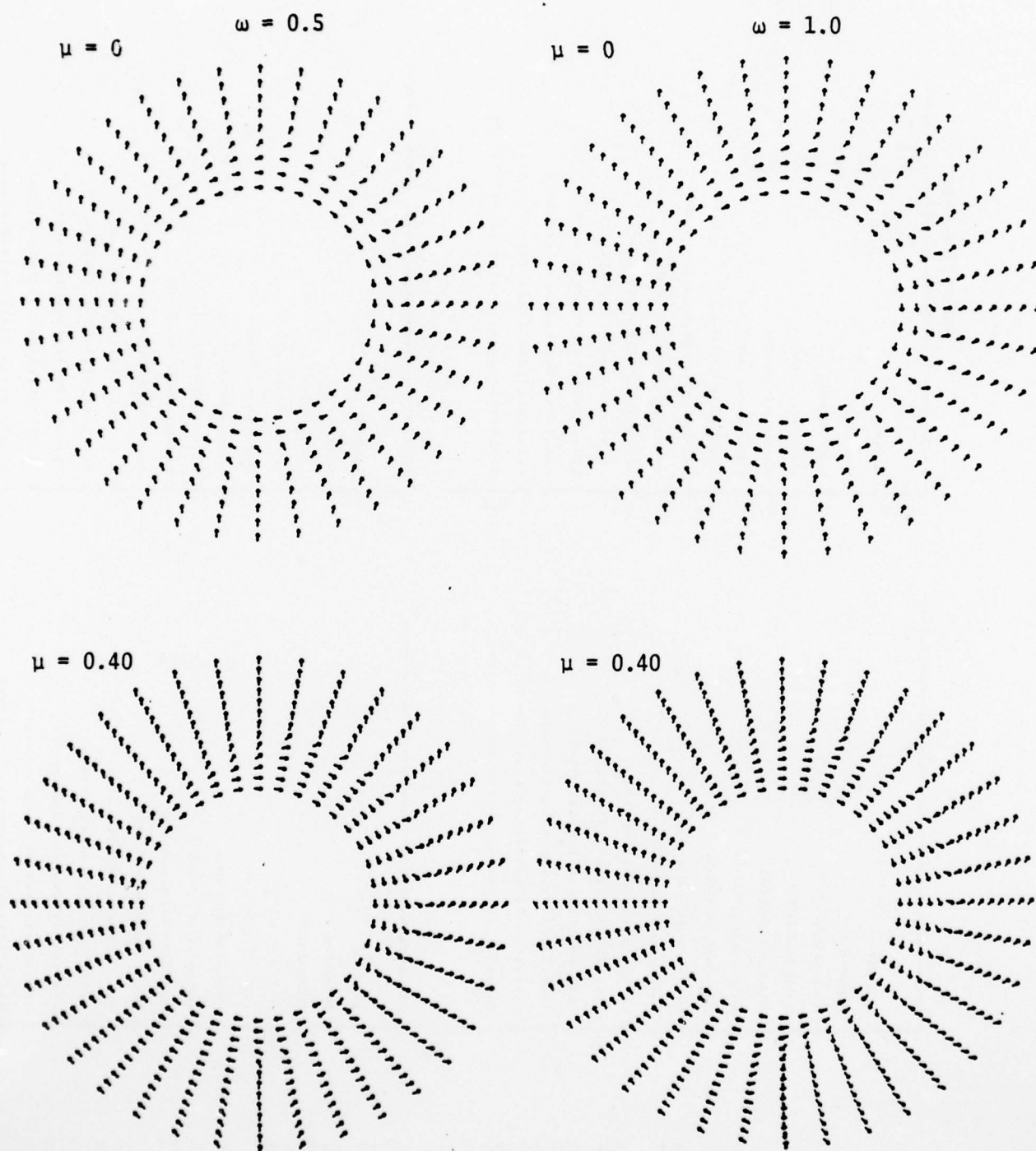


Fig. B3. Continued.

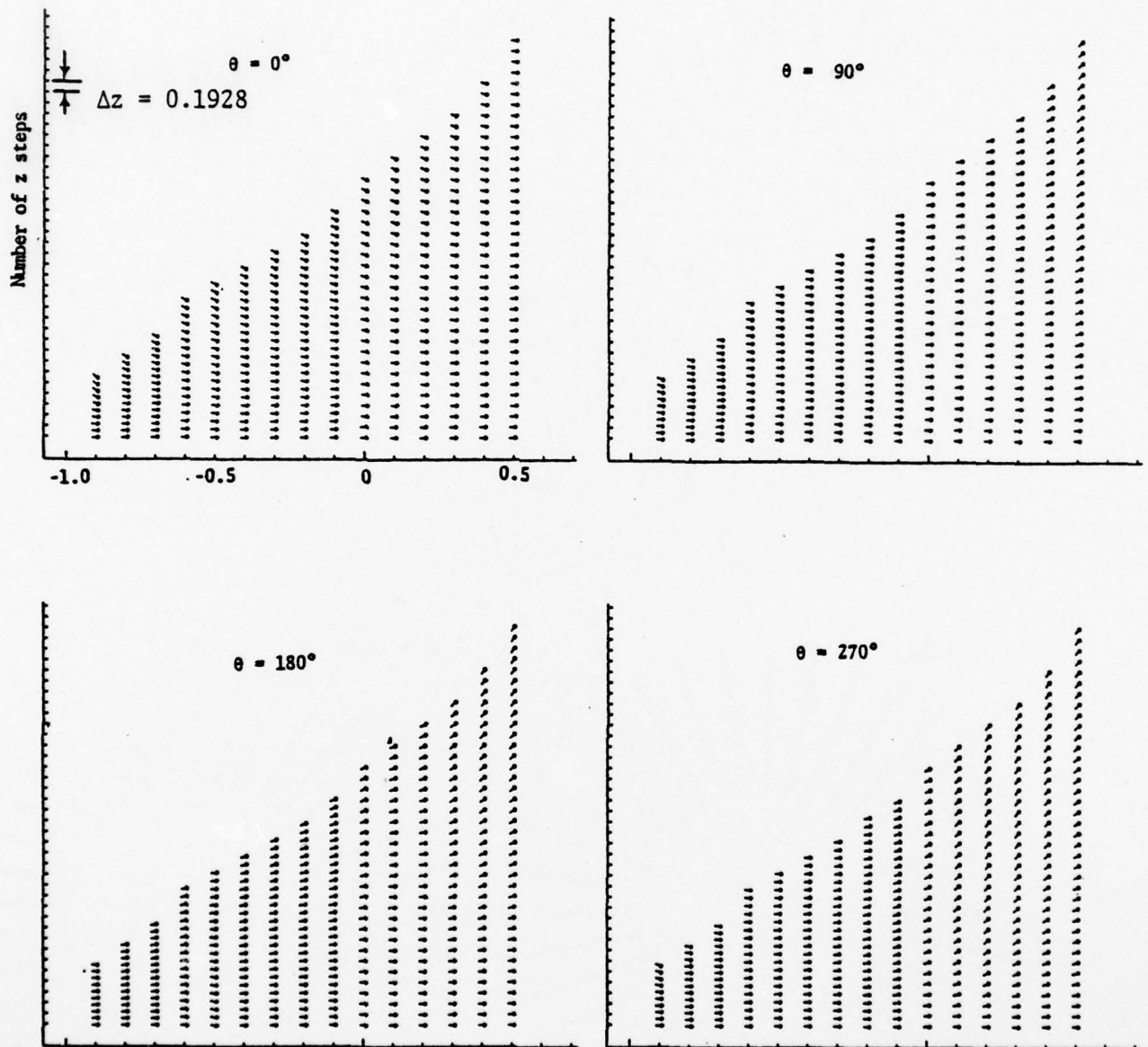


Fig. B4. Meridional-plane flow pattern,  $\alpha = 6^\circ$ ,  $\omega = 0.5$ .

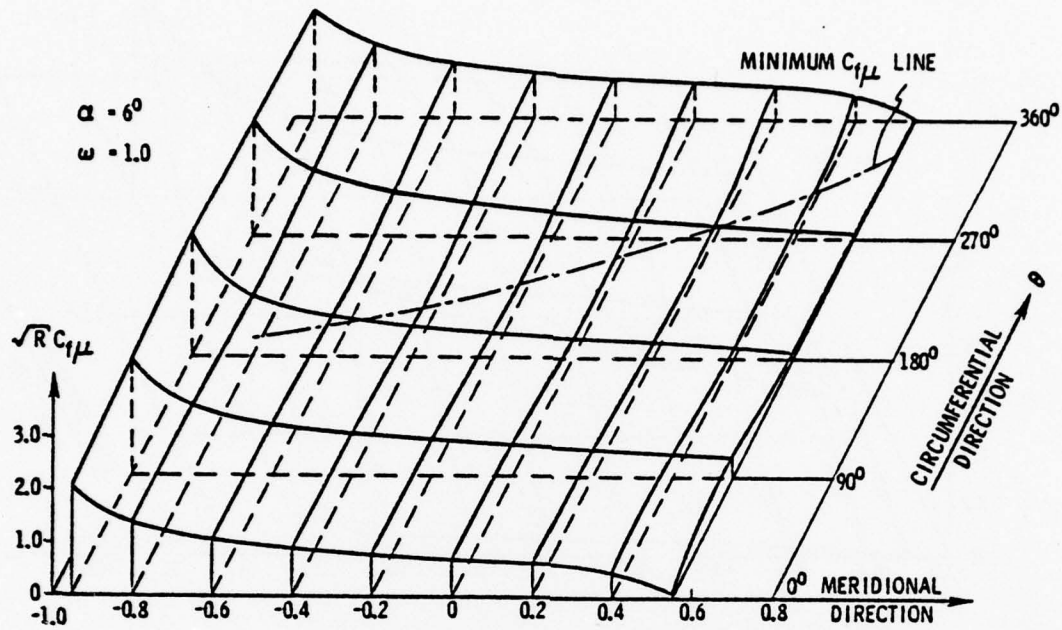


Fig. B5. Meridional skin friction.

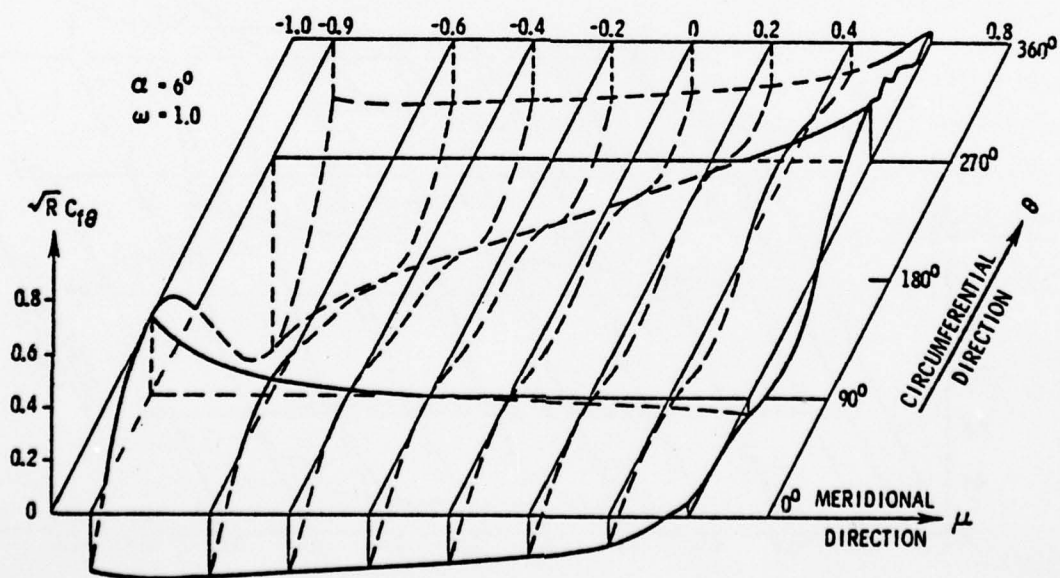


Fig. B6. Circumferential skin friction.

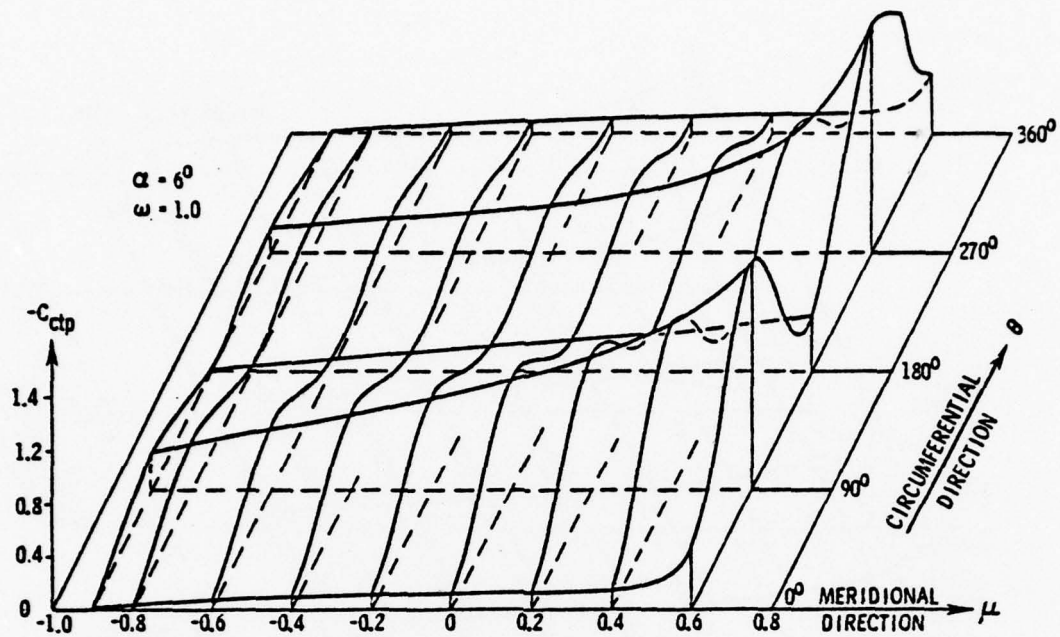


Fig. B7. Centrifugal pressure.

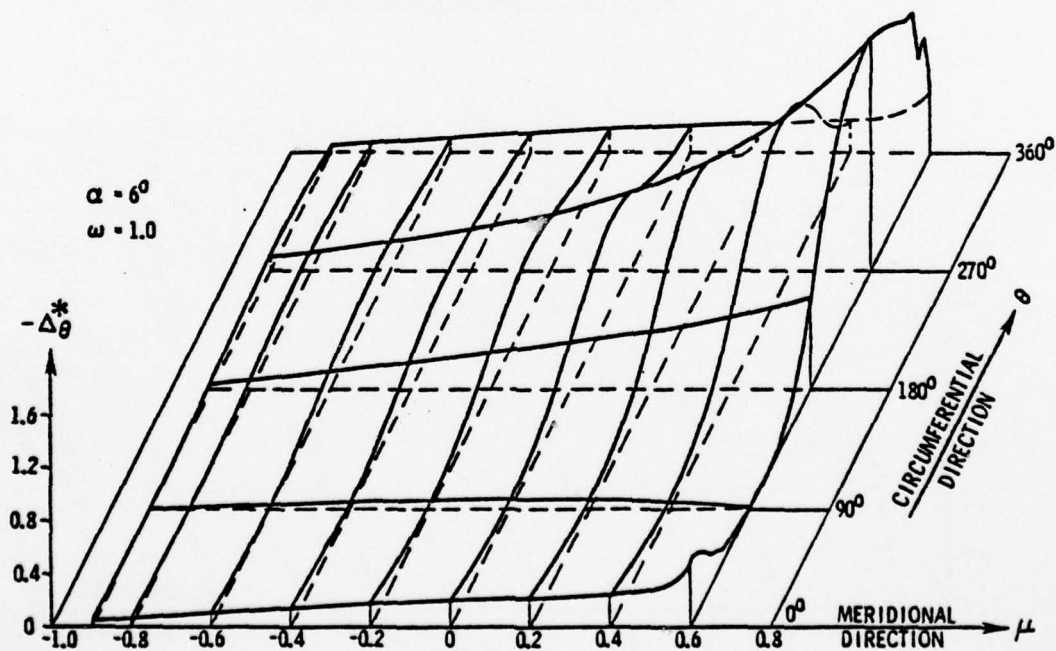


Fig. B8. v-velocity displacement thickness.



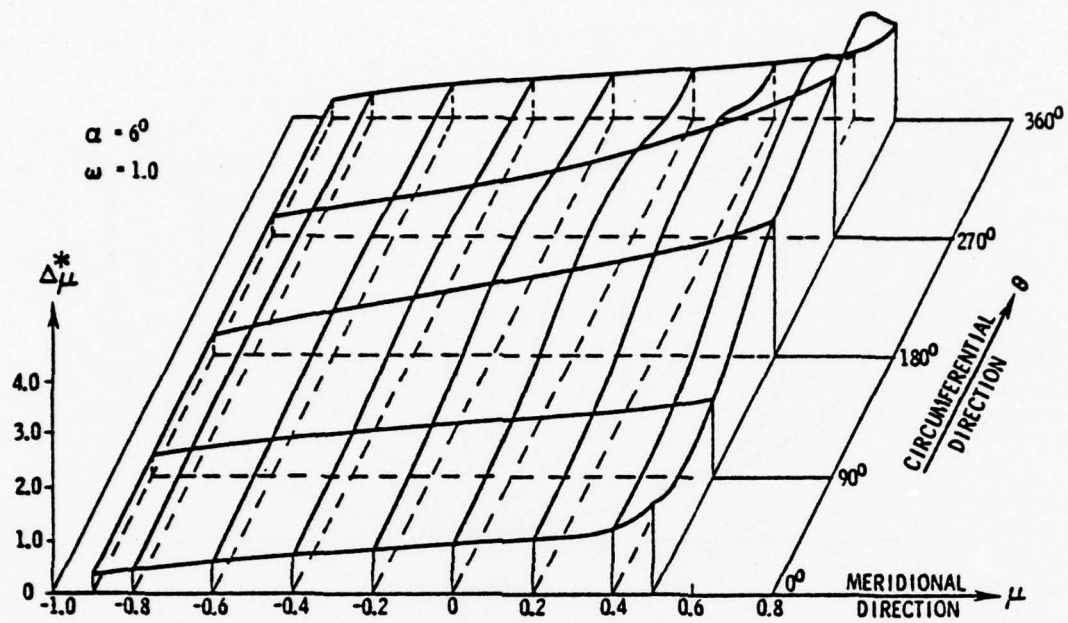


Fig. B9. u-velocity displacement thickness.

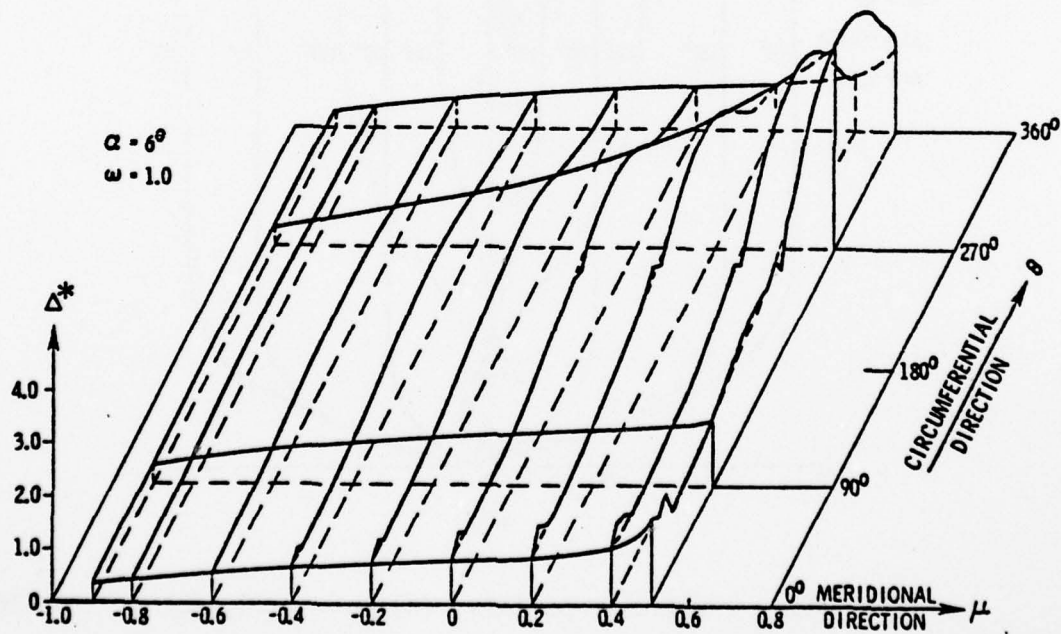


Fig. B10. Total displacement thickness.

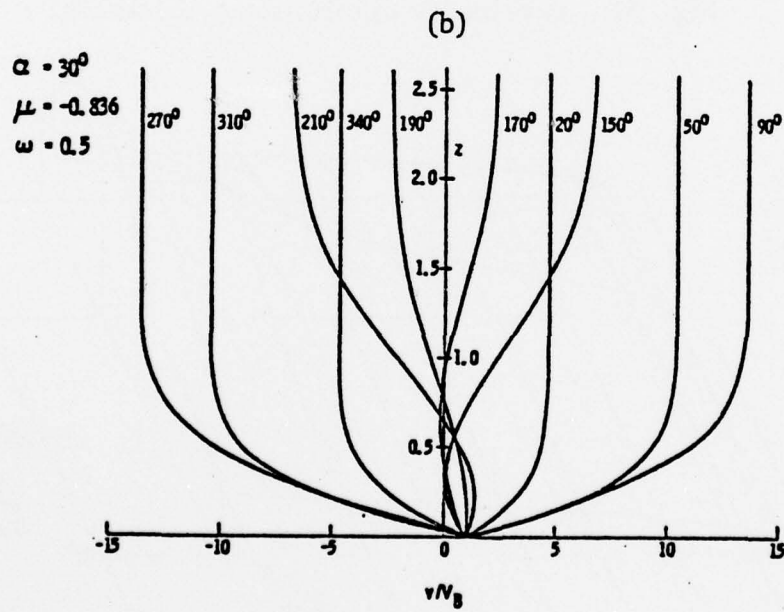
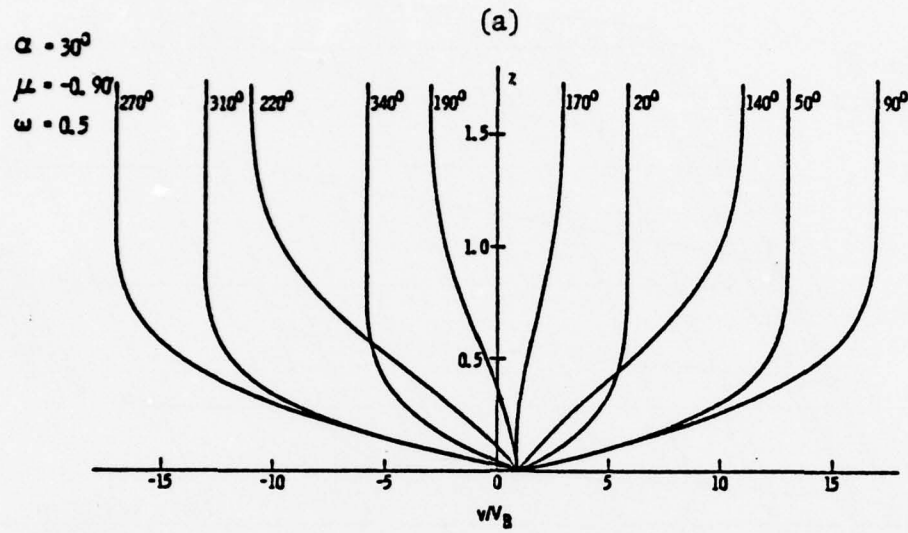


Fig. B11.  $v$ -velocity profile. (a)  $\mu = -0.90$ , (b)  $\mu = -0.836$ .

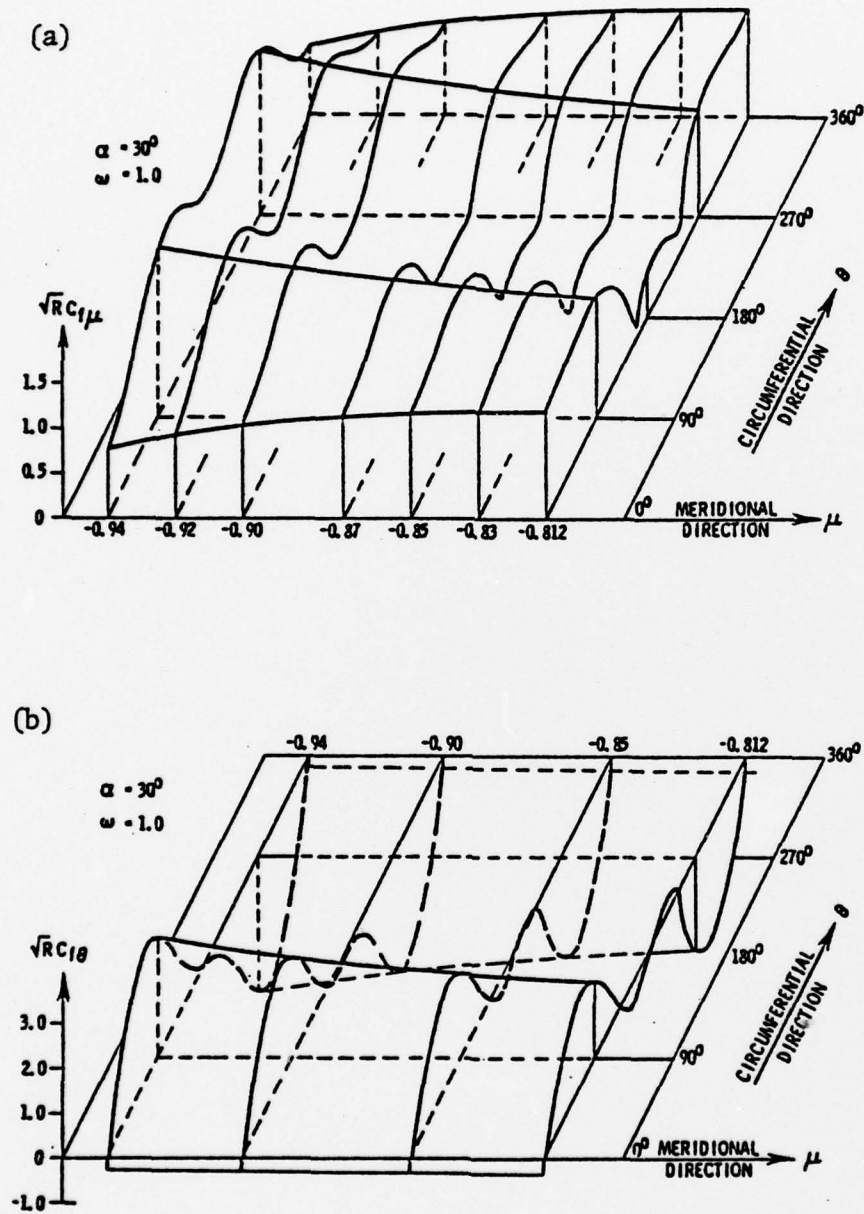


Fig. B12. Skin friction distribution. (a) Meridional skin friction, (b) Circumferential skin friction.